Cell Metabolism

Article

Vps37a regulates hepatic glucose production by controlling glucagon receptor localization to endosomes

Graphical abstract

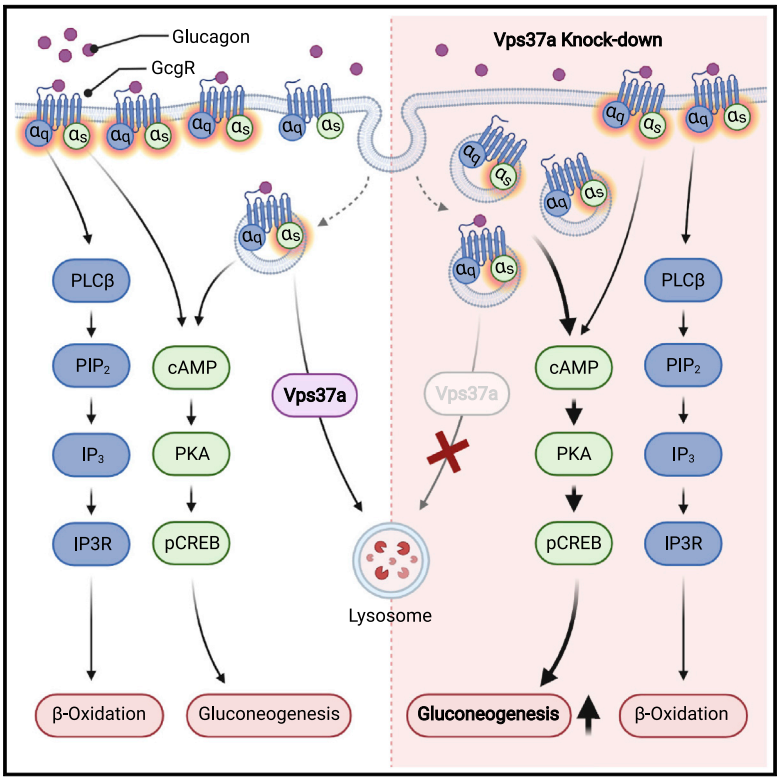

Highlights

- Vps37a controls the intracellular trafficking of glucagon receptor to lysosomes
- Vps37a depletion accumulates Gcgr at early endosomes and enhances Gαs signaling
- Vps37a KD uncouples Gcgr signaling to hepatic glucose production from β-oxidation
- Liver Vps37a and ESCRT-I are potential targets for blood glucose regulation in diabetes

Authors

Revathi Sekar, Karsten Motzler, Yun Kwon, ..., Marta Miaczynska, Stephan Herzig, Anja Zeigerer

Correspondence

anja.zeigerer@helmholtz-muenchen.de

In brief

Sekar et al. report on a novel mechanism to uncouple differential signaling outcomes of the glucagon receptor in the liver. Changing the localization of the receptor by targeting endosomal Vps37a alters glucose production and usage downstream of glucagon, without affecting lipid metabolism.

Sekar et al., 2022, Cell Metabolism *34*, 1824–1842
November 1, 2022
https://doi.org/10.1016/j.cmet.2022.09.022

CellPress

CellPress
OPEN ACCESS

Cell Metabolism

Article

Vps37a regulates hepatic glucose production by controlling glucagon receptor localization to endosomes

Revathi Sekar,[1,2,3,15] Karsten Motzler,[1,2,3,15] Yun Kwon,[1,2,3] Aaron Novikoff,[3,4] Julia Jülg,[5] Bahar Najafi,[1,2,3] Surui Wang,[1,2,3] Anna-Luisa Warnke,[3,6,7] Susanne Seitz,[1,2,3] Daniela Hass,[1,2,3] Sofiya Gancheva,[3,8,9] Sabine Kahl,[3,8,9] Bin Yang,[10] Brian Finan,[10] Kathrin Schwarz,[11] Juergen G. Okun,[11] Michael Roden,[3,8,9] Matthias Blüher,[12] Timo D. Müller,[3,4] Natalie Krahmer,[3,4] Christian Behrends,[5] Oliver Plettenburg,[3,6,7] Marta Miaczynska,[13] Stephan Herzig,[1,2,3,14] and Anja Zeigerer[1,2,3,16,*]

[1]Institute for Diabetes and Cancer, Helmholtz Munich, Neuherberg, Germany
[2]Joint Heidelberg-IDC Translational Diabetes Program, Inner Medicine 1, University Hospital, Heidelberg, Germany
[3]German Center for Diabetes Research, Neuherberg, Germany
[4]Institute for Diabetes and Obesity, Helmholtz Munich, Neuherberg, Germany
[5]Munich Cluster for Systems Neurology, Ludwig-Maximilians-University, Munich, Germany
[6]Institute of Medicinal Chemistry, Helmholtz Munich, Neuherberg, Germany
[7]Institute of Organic Chemistry, Center of Biomolecular Research, Leibniz University, Hannover, Germany
[8]Division of Endocrinology and Diabetology, Medical Faculty, Heinrich Heine University, Düsseldorf, Germany
[9]Institute for Clinical Diabetology, Leibniz Center for Diabetes Research at Heinrich Heine University, Düsseldorf, Germany
[10]Novo Nordisk Research Center, Indianapolis, IN, USA
[11]Department of General Paediatrics, Division of Neuropaediatrics and Metabolic Medicine, University Children's Hospital, Heidelberg University, Heidelberg, Germany
[12]Helmholtz Institute for Metabolic, Obesity and Vascular Research (HI-MAG), Helmholtz Munich at the University of Leipzig and University Hospital Leipzig, Leipzig, Germany
[13]Laboratory of Cell Biology, International Institute of Molecular and Cell Biology, Warsaw, Poland
[14]Chair Molecular Metabolic Control, Technical University Munich, Munich, Germany
[15]These authors contributed equally
[16]Lead contact
*Correspondence: anja.zeigerer@helmholtz-muenchen.de
https://doi.org/10.1016/j.cmet.2022.09.022

SUMMARY

During mammalian energy homeostasis, the glucagon receptor (Gcgr) plays a key role in regulating both glucose and lipid metabolisms. However, the mechanisms by which these distinct signaling arms are differentially regulated remain poorly understood. Using a Cy5-glucagon agonist, we show that the endosomal protein Vps37a uncouples glucose production from lipid usage downstream of Gcgr signaling by altering intracellular receptor localization. Hepatocyte-specific knockdown of Vps37a causes an accumulation of Gcgr in endosomes, resulting in overactivation of the cAMP/PKA/p-Creb signaling pathway to gluconeogenesis without affecting β-oxidation. Shifting the receptor back to the plasma membrane rescues the differential signaling and highlights the importance of the spatiotemporal localization of Gcgr for its metabolic effects. Importantly, since Vps37a knockdown in animals fed with a high-fat diet leads to hyperglycemia, although its overexpression reduces blood glucose levels, these data reveal a contribution of endosomal signaling to metabolic diseases that could be exploited for treatments of type 2 diabetes.

INTRODUCTION

Hepatic glucose production (HGP) is a key physiological process in systemic glucose homeostasis (Petersen et al., 2017). During fasting, glucagon stimulates HGP by activating gluconeogenesis and glycogenolysis to maintain euglycemia and provide fuels for glucose consuming organs, such as the brain. Overactivation of those pathways, as observed in patients with type 2 diabetes (T2D), contributes to fasting hyperglycemia and insulin resistance (IR) (Rizza, 2010; Samuel and Shulman, 2016). However, the cell-biological mechanisms that ensure proper control of HGP remain poorly understood.

The glucagon receptor (GCGR), a class B G protein-coupled receptor (GPCR), is the principal regulator of glucagon action in the liver (Müller et al., 2017; Petersen et al., 2017; Zeigerer et al., 2021). Its activation through glucagon binding at the plasma membrane (PM) stimulates a complex signaling cascade in which the $G_{\alpha s}$ subunit initiates cAMP-mediated induction of gluconeogenic

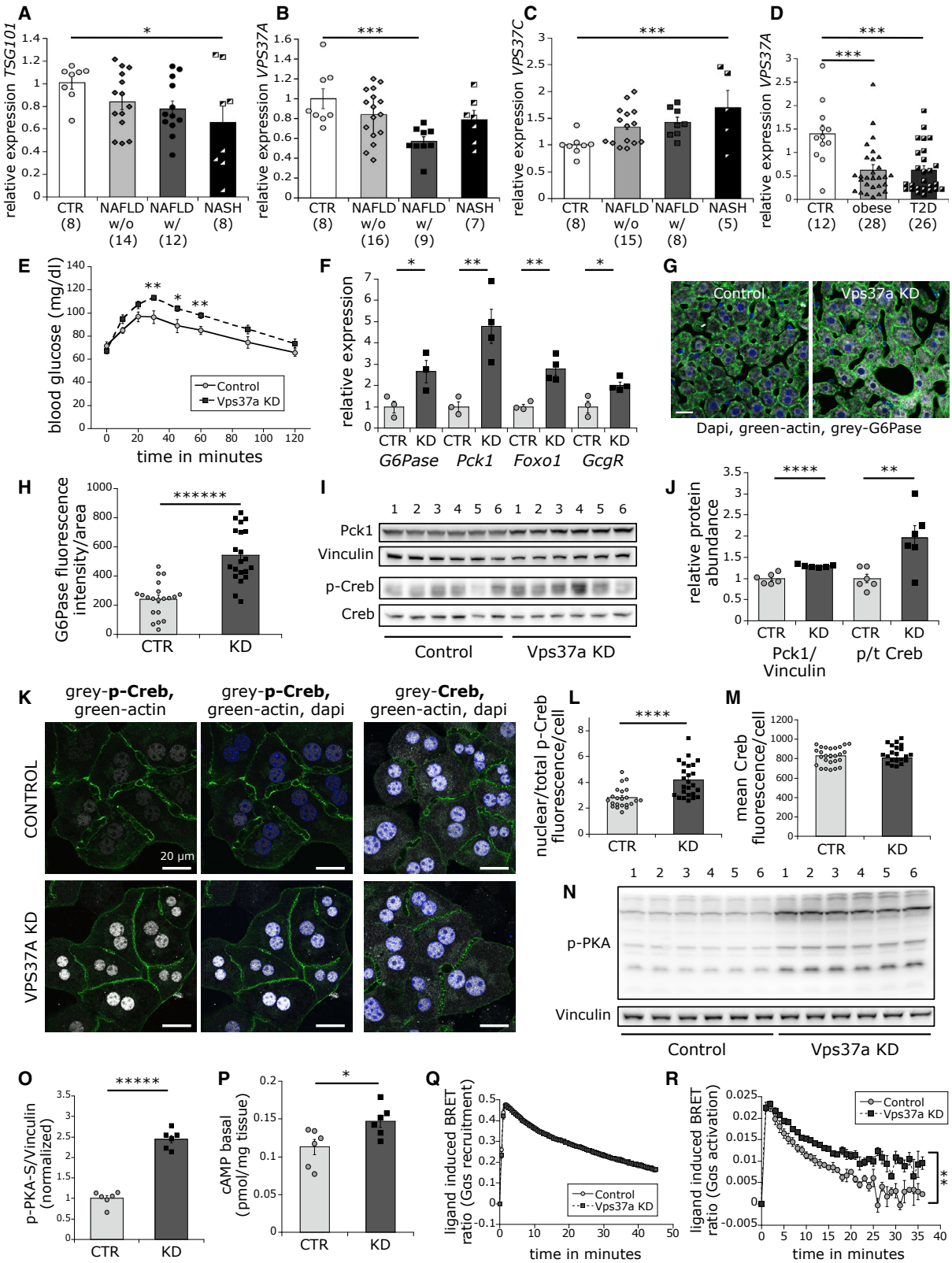

Figure 1. Depletion of Vps37a in liver causes increased glucose production and activation of the basal cAMP/PKA/p-Creb pathway

(A–C) Relative expression of *TSG101* (A), *VPS37A* (B), and *VPS37C* (C) in liver of patients with NALFD ± steatosis (n = 8–16), NASH (n = 5–8), and healthy controls (n = 8).

(legend continued on next page)

genes, *glucose-6-phosphatase* (*G6PC*) and *phosphoenolpyruvate kinase* (*PCK1*), by activating the protein kinase A (PKA)/cAMP responsive element binding (CREB) protein signaling pathway. On the other hand, the $G_{\alpha q}$ subunit acts through phospholipase C_ε (PLC_ε)-mediated inositol trisphosphate (IP_3) production and stimulates β-oxidation of fatty acids via induction of INSP3R1-dependent calcium efflux from the endoplasmic reticulum to the mitochondria (Perry et al., 2020; Petersen et al., 2017; Zeigerer et al., 2021). The combined downstream effect of GCGR signaling on glucose production and lipid usage limits the potential of GCGR as a target for T2D, as the use of inhibitors to reduce hyperglycemia is associated with the development of fatty liver and dyslipidemia (Sammons and Lee, 2015; Scheen et al., 2017). Without a detailed mechanistic understanding of how the different signaling functions are regulated, however, targeted strategies remain a challenge.

Despite the classical view that GPCR-activated signaling occurs only at the PM, evidence is now emerging that shows G-protein signaling from class A GPCRs in various intracellular compartments, revealing an additional level of complexity in signal regulation (Eichel and von Zastrow, 2018; Sutkeviciute and Vilardaga, 2020). Upon external ligand binding, GPCRs are phosphorylated by GPCR kinases, which recruit cytosolic β-arrestins, leading to receptor internalization to endosomes for either lysosomal degradation or resensitization by recycling to the PM (Eichel and von Zastrow, 2018). Altering this intracellular trafficking behavior has revealed that similar to receptor tyrosine kinases (Miaczynska, 2013), a spatiotemporal regulation of GPCR signaling occurs (Tsvetanova and von Zastrow, 2014). Whether this is similarly true for the metabolically relevant class B GPCRs, such as the Gcgr, is unknown. Given the important role of these receptors in T2D and non-alcoholic fatty liver disease (NAFLD), a better characterization of their intracellular signaling is needed. In addition, the significance of endosomal sorting proteins in the spatiotemporal dynamics of these receptors and the consequences for systemic metabolism remain completely unexplored.

Here, we show that the vacuolar protein sorting 37a (Vps37a) regulates HGP by controlling lysosomal degradation of Gcgr. Vps37a is a member of the endosomal sorting complexes required for the transport (ESCRT)-I complex (Bache et al., 2004), playing a key role in sorting membrane receptors to degradation, thereby contributing to signal termination (Szymanska et al., 2018). Our study shows that the reduction of Vps37a in hepatocytes causes endosomal accumulation of Gcgr while reducing its presence in lysosomes, leading to preferential activation of HGP without affecting fatty acid β-oxidation. These data indicate a unique function of Vps37a in Gcgr trafficking, highlighting a thus far unknown role in regulating metabolic signaling of Gcgr.

RESULTS

VPS37A is downregulated in patients with diabetes and NAFLD

Given the proposed role of the ESCRT-I machinery in NAFLD and progression to non-alcoholic steatohepatitis (NASH) (Zhao et al., 2017), we investigated ESCRT-I components in the regulation of liver metabolism. ESCRT-I is a heterotetrameric complex comprising tumor susceptibility gene 101 (Tsg101), Vps28, Vps37 (a-d), and one auxiliary protein (UBAP-1) (Hurley, 2010; Schmidt and Teis, 2012). Thus, we compared the mRNA levels of *TSG101*, *VPS28*, *VPS37A*, *VPS37B*, and *VPS37C* in livers of healthy individuals with those of patients with NAFLD with or without hepatocyte ballooning and NASH (Koliaki et al., 2015). Expression of *VPS37A* was significantly reduced (43%) specifically in patients with severe NAFLD, whereas *TSG101* and *VPS37C* only showed a slight decrease or increase, respectively, in patients with NASH (Figures 1A–1C), whereas *VPS28* and *VPS37B* were unaffected (Figures S1A and S1B). *VPS37A* expression correlated positively with *PGC1α* and negatively with hepatocellular lipid content, thiobarbituric acid, 8-oxoguanosine, and interleukin-6 across the entire patient cohort (Table S1). These data suggest a specific role for VPS37A in NAFLD, in which low levels of VPS37A were associated with an impairment of liver health.

As the severity of NAFLD is often linked to an increased incidence of T2D (Mantovani et al., 2018), we screened the expression of ESCRT-I in a cohort of patients with obesity and T2D compared with healthy controls. Consistent with the first patient cohort, *VPS37A* expression was strongly reduced (56%) in patients with both obesity and T2D (Figure 1D), together with *VPS37B*; however, other ESCRT-I members were unchanged (Figures S1C–S1G). We did not detect *VPS37D* in both cohorts, indicating no expression in liver. *VPS37A* levels were negatively correlated with body mass index (BMI); fasting plasma insulin; subcutaneous, visceral, liver, and body fat; total cholesterol; triglyceride (TG); and leptin levels in these patients (Table S1), indicating a link of hepatic *VPS37A* levels with lipid and glucose homeostasis in humans. Altogether, these data highlight an inverse correlation between *VPS37A* expression levels and clinically impaired metabolism in humans, suggesting a crucial role for VPS37A in T2D and NAFLD.

(D) Relative expression of *VPS37A* in liver of patients with obesity (n = 28), diabetes (n = 26), and healthy controls (n = 12).
(E) ipPTT after 16 h starvation (n = 6).
(F) Relative gluconeogenic gene expression.
(G and H) (G) Representative single confocal liver sections stained for G6pc (gray), phalloidin (green), and DAPI (blue), quantified in (H) (n = 20–21 cells).
(I and J) (I) Representative western blots for Pck1, basal p-, and t-Creb in liver and quantification in (J).
(K–M) (K) Representative single confocal hepatocyte sections stained for p- and t-Creb (gray), phalloidin (green), and DAPI, quantified in (L) and (M) (n = 21–26).
(N and O) (N) Representative western blot for p-PKA substrates, quantified in (O).
(P) Basal liver cAMP levels (n = 6).
(Q) Temporal resolution of ligand-induced mini-$G\alpha_s$-Nluc recruitment to GFP-tagged GcgR in HEK cells.
(R) Temporal resolution of ligand-induced GTP-Gα formation with Gβγ-BERKY3 sensor in untagged GcgR-positive HEK cells. Data normalized to individual vehicle control and baseline.
All animals and hepatocytes treated with control (CTR) or Vps37a (KD) LNPs or siRNAs (mean ± SEM). *p < 0.05, **p < 0.01, ***p < 0.001, ****p < 0.0001, *****p < 0.00001 by two-tailed unpaired Student's t test and two-way ANOVA (A–D).

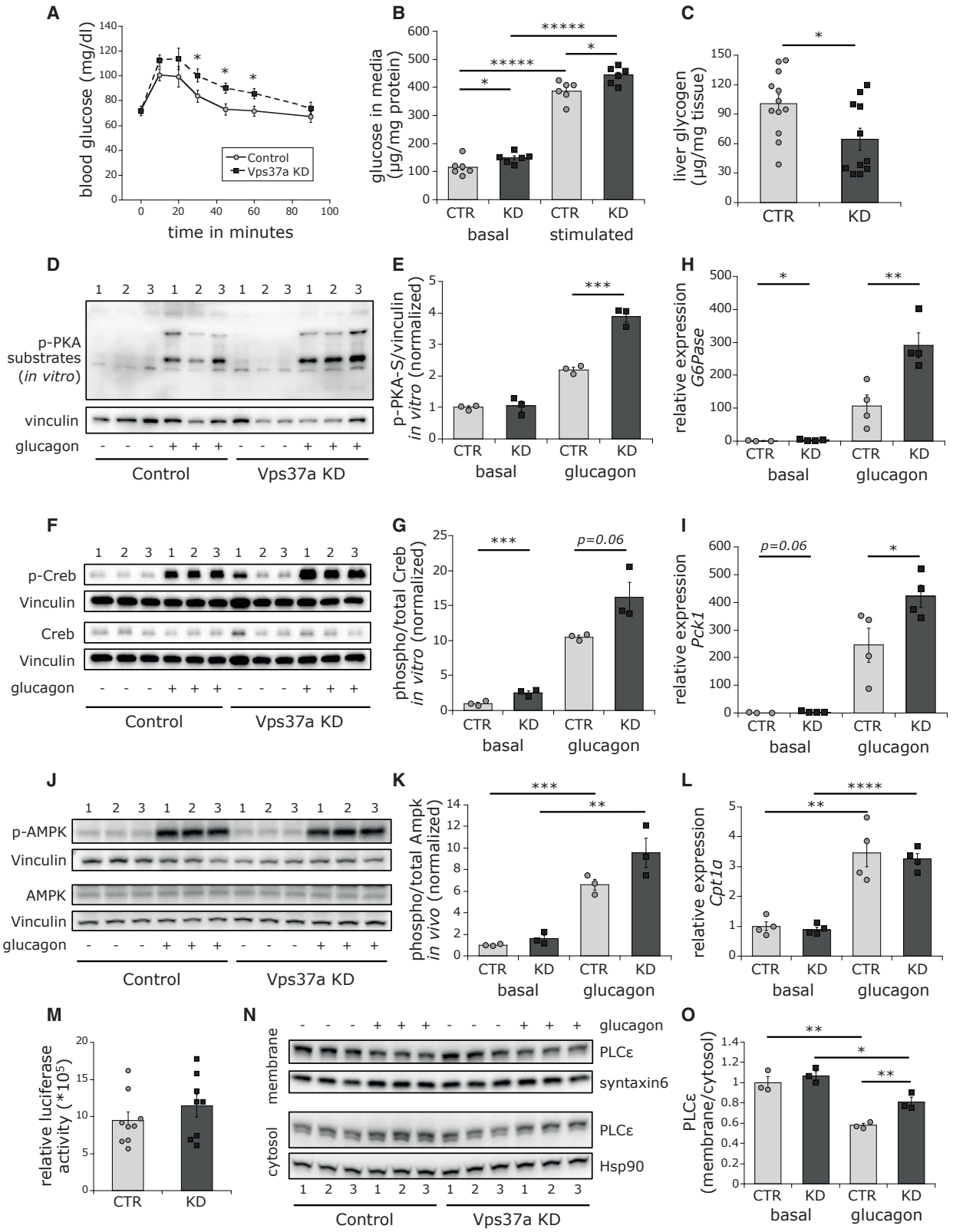

Figure 2. Vps37aKD leads to overactivated glucagon signaling

(A) Glucagon tolerance test in mice (n = 6).

(B) Glucose secretion from primary hepatocytes (n = 6).

(legend continued on next page)

Vps37a depletion enhances gluconeogenesis and liver glucose production

To explore the metabolic role of Vps37a, we silenced Vps37a *in vivo* in mouse hepatocytes by tail vein injection of lipid nanoparticles (LNPs) containing Vps37a siRNA (Seitz et al., 2019; Zeigerer et al., 2012, 2015). A maximal knockdown (KD) efficiency of 80% was achieved after 11 days (Figures S1H and S1I), as reported for other LNPs (Akinc et al., 2010; Bogorad et al., 2014; Seitz et al., 2019; Zeigerer et al., 2012). Reduction of Vps37a did not affect liver/body weight ratio, glucose tolerance, glucose-stimulated plasma insulin levels, or insulin tolerance (Figures S1J–S1M). Furthermore, protein kinase B (Akt) activation after insulin stimulation (Figures S1N and S1O) and insulin receptor (Insr)-β protein levels remained unchanged in Vps37aKD liver (Figure S1P). However, reduction of Vps37a caused a significant increase in HGP during pyruvate and glycerol tolerance tests (Figures 1E and S1Q), without changing plasma glucagon levels (Figure S1R), suggesting a preferential role of Vps37a in HGP. There was a significant increase in the mRNA and protein levels of the gluconeogenic enzymes G6Pase and Pck1 upon Vps37aKD *in vivo* (Figures 1F–1J), further supporting an activation of glucose production. Upregulation of gluconeogenesis was accompanied by increased Forkhead transcription factor XO 1 (*Foxo1*) and *Gcgr* expression (Figure 1F), without altering *Creb* and its downstream target *Pgc1α* or the glycolytic genes *Gck* and *Pklr* (Figure S1S). To test whether the impact on gluconeogenesis was cell autonomous, we performed KD of Vps37a in isolated primary hepatocytes (Zeigerer et al., 2015) and observed an 80% reduction in mRNA and protein levels (Figures S1T–S1V). Vps37aKD also caused a significant increase in basal *G6Pase* and *Pck1* levels, without changing *Gck* and *Pklr in vitro* (Figure S1T), further supporting a hepatocyte-specific effect on activation of gluconeogenesis.

To determine the underlying mechanism by which Vps37a reduction induces HGP, we investigated the phosphorylation of Creb, which is known to induce transcriptional activation of gluconeogenic genes (Altarejos and Montminy, 2011; Herzig et al., 2001). Interestingly, we observed a significant increase in basal p-Creb in Vps37a-depleted livers (Figures 1I and 1J), which was in line with upregulated gluconeogenic genes. This was further confirmed in primary hepatocytes, wherein staining for p-Creb showed a significantly higher nuclear localization after depletion of Vps37a (Figures 1K–1M), hinting at overactivated Creb signaling even in the basal state. Creb phosphorylation is achieved by the cAMP/PKA signaling pathway. Thus, we tested whether Vps37aKD altered PKA activation and cAMP levels in mouse livers. Remarkably, we found a 2.5-fold increase in the abundance of cAMP-dependent p-PKA substrates (Figures 1N and 1O) and a 20% increase in cAMP amounts (Figure 1P). The increase in cAMP levels was not attributed to changes in ligand-receptor interaction, as ligand-induced GCGR activation was fully intact measured by direct colocalization of $G_{\alpha s}$ and GCGR using MiniGs in control and VPS37AKD HEK293T cells (Figure 1Q). As MiniGs form stable complexes with the receptor that may not dissociate easily, these results reflect ligand-induced receptor conformational changes that allow $G_{\alpha s}$ access to the receptor, rather than the transient dynamics of active $G_{\alpha s}$ signaling itself (Wan et al., 2018). Thus, we determined the total amount of GTP-bound Gα produced using the βγ-BERKY3 sensor (Figure 1R), which measures ligand-induced dissociation of Gα subunits from the βγ-subunits and indirectly represents active $G_{\alpha s}$ signaling (Maziarz et al., 2020). Interestingly, despite the intact ligand-receptor conformational dynamics allowing equal Gα access (Figure 1Q), VPS37AKD enhanced GTP-Gα production through spatial compartmentalization (Figure 1R).

Reduction of Vps37a causes overactivation of glucagon signaling toward the cAMP/PKA/Creb pathway

The accumulation of basal cAMP along with PKA and p-Creb activation in Vps37aKD livers suggests a regulatory role for Vps37a in glucagon signaling. Therefore, to test whether Vps37a modulates glucagon responsiveness, we performed a glucagon stimulation test (Longuet et al., 2008) in mice. Vps37aKD mice exhibited elevated blood glucose levels 30–60 min after glucagon stimulation and an elevated area under the curve (Figures 2A and S2A), indicating increased glucagon-induced activation of HGP. This was confirmed in primary mouse hepatocytes, where glucose production was enhanced under basal and glucagon-stimulated conditions, supporting a cell-autonomous effect on gluconeogenesis (Figure 2B). Consistent with overactivation of glucagon signaling and a consequent initiation of glycogen breakdown in the liver (Habegger et al., 2010), liver glycogen content was significantly reduced (Figure 2C). As Vps37aKD already caused increased basal p-PKA substrates and p-Creb (Figures 1I–1N), we wondered whether this induction could be further enhanced by glucagon stimulation. Indeed, glucagon treatment induced an even greater increase in p-PKA substrates and p-Creb levels in primary hepatocytes (Figures 2D–2G) and mouse liver (Figures S2B–S2E), suggesting that Vps37a depletion primes glucagon signaling toward a stronger response. In agreement, glucagon stimulation further increased *G6pc* and *Pck1* expressions in Vps37a-depleted hepatocytes (Figures 2H and 2I). Interestingly, glucagon-stimulated reduction in p-Foxo levels was unaltered in Vps37aKD livers, showing that upregulation of the gluconeogenic pathway was indeed mediated by enhanced PKA/Creb signaling (Figures S2D and S2F). Importantly, the increase in PKA activity

(C) Liver glycogen levels (n = 11–12).
(D–G) (D and F) Representative western blots for p-PKA substrates and p- and t-Creb in primary hepatocytes after glucagon stimulations and quantifications in (E) and (G) (n = 3).
(H and I) Relative expression of *G6Pase* (H) and *Pck1* (I) in glucagon-stimulated primary hepatocytes.
(J and K) (J) Representative western blots for p-and t-AMPK in liver of glucagon-injected mice and quantifications in (K) (n = 3).
(L) Relative expression of *Cpt1a* in hepatocytes after glucagon stimulations (n = 3–4).
(M) Relative ATP levels (n = 8–9).
(N and O) (N) Representative western blots of cytosol and membrane liver fractions for Plcε of glucagon-injected mice (n = 3) (O) with quantification relative to cytosolic (Hsp90) or membrane (syntaxin 6) proteins in (N) (n = 3).
All animals and hepatocytes treated with control (CTR) and Vps37a (KD) LNPs or siRNAs and injected or stimulated with glucagon (mean ± SEM). *p < 0.05, **p < 0.01, ***p < 0.001, ****p < 0.0001, and *****p < 0.00001 by two-tailed unpaired Student's t test.

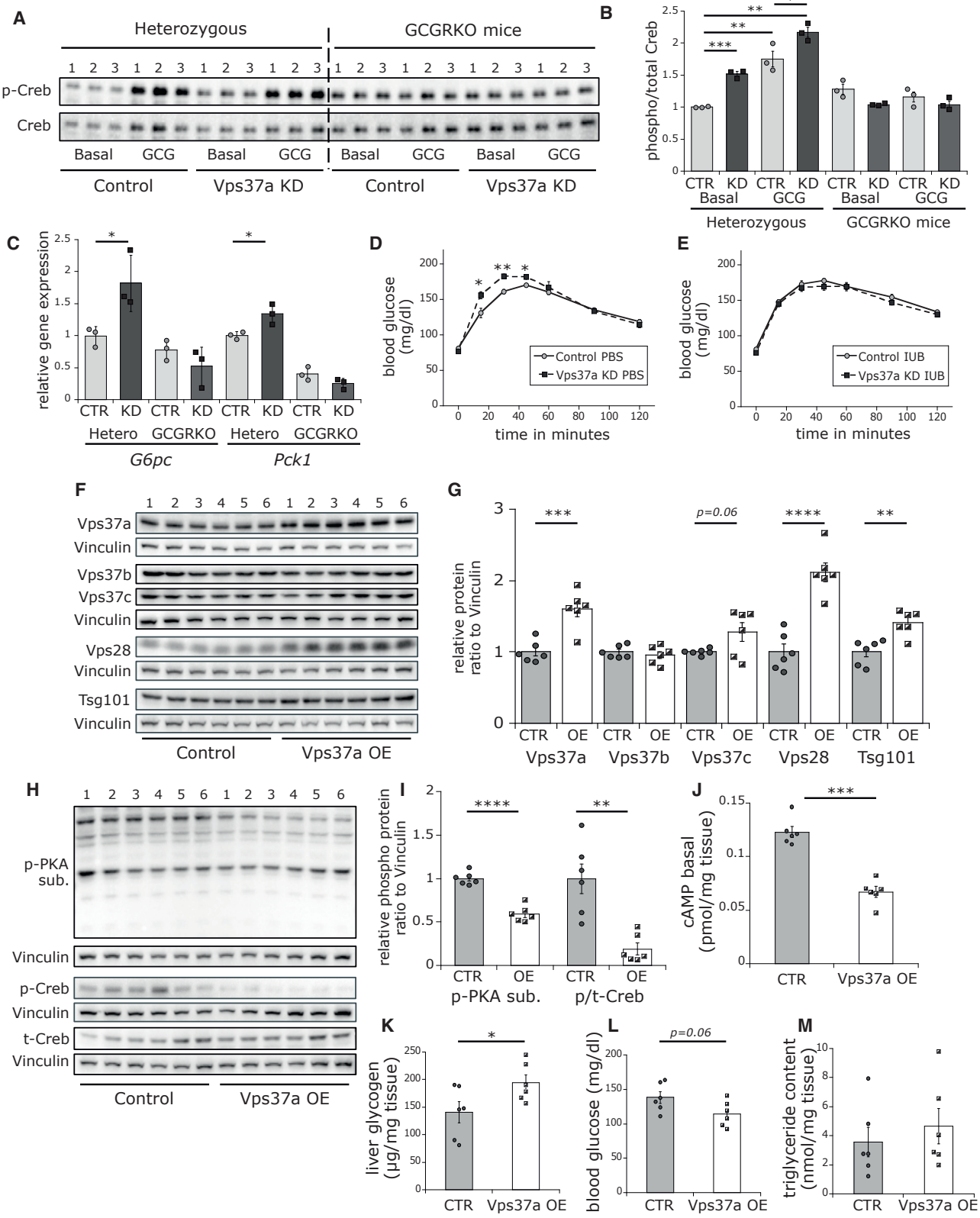

Figure 3. Vps37a regulates cAMP/p-Creb signaling via Gcgr

(A and B) (A) Representative western blot for p- and t-Creb in hepatocytes from hetero- and homozygous liver-specific *Gcgr*$^{-/-(liver)}$ KO mice stimulated with glucagon and quantification in (B) (n = 3).

(legend continued on next page)

was not due to an impairment of cAMP-depleting phosphodiesterase function, as forskolin treatments induced the same levels of p-PKA substrates (Figures S2G and S2H), indicating that the induction of PKA was due to enhanced cAMP production and upstream signaling.

Activation of glucagon signaling was specific for the cAMP/PKA/p-Creb pathway, as we did not observe alterations in the phosphorylation of AMP-activated PK (AMPK) or acetyl-CoA carboxylase (ACC) (Kimball et al., 2004; Longuet et al., 2008; Figures 2J, 2K, S2I, and S2J) upon glucagon stimulation *in vivo*, and consequently, no changes in carnitine palmitoyltransferase 1α (*Cpt1*α) gene expression (Figure 2L) *in vitro*. This is consistent with unchanged ATP levels (Figure 2M), showing that the induction of cAMP upon Vps37aKD is insufficient to activate AMPK.

Although the translocation of PLC_{ε} from the PM to the cytosol was reduced by 20% upon glucagon stimulation (Figures 2N and 2O), this decrease had no influence on the phosphorylation levels of downstream calcium/calmodulin-dependent PK type II (CaMKII) (Figures S2I and S2K), in line with the fact that the fraction of the receptor occupied and not the protein levels are important for signaling efficacy (Berg and Clarke, 2018; Bush et al., 2016). Importantly, we observed no changes in liver and serum lipid parameters upon Vps37aKD (Table S2), indicating no alterations in Gcgr signaling to lipid metabolism. Moreover, serum alanine levels were significantly reduced, consistent with an increased flux toward hepatic gluconeogenesis (Table S3). In conclusion, loss of Vps37a activates basal and glucagon-mediated cAMP/PKA/p-Creb signaling without affecting AMPK and CaMKII activation, leading to a subsequent selective increase in gluconeogenesis and HGP without altering lipid homeostasis.

Vps37a KD effects are Gcgr dependent

The major signaling pathway in the liver responsible for cAMP-dependent activation of p-Creb and concomitant induction of gluconeogenesis is regulated by Gcgr (Authier and Desbuquois, 2008; Habegger et al., 2010; Janah et al., 2019). The observed induction of the cAMP/PKA/p-Creb pathway by Vps37aKD and consequent increase in gluconeogenic genes and glucose output thus indicate a potential role for Vps37a in Gcgr signaling. To determine whether the metabolic effects of Vps37a are Gcgr dependent, we isolated primary hepatocytes from liver-specific Gcgr knockout (KO) mice ($Gcgr^{-/-liver}$) and analyzed whether Vps37aKD could activate gluconeogenesis. A 50% reduction in *Vps37a* in *Gcgr* KO hepatocytes induced increased basal and glucagon-stimulated p-Creb activation as well as *G6pc* and *Pck1* expression in hetero- but not in homozygous $Gcgr^{-/-liver}$ hepatocytes (Figures 3A–3C), confirming Gcgr dependence. Importantly, this was Gcgr specific, as the protein levels of another GPCR and driver of cAMP levels in the liver, the β2-adrenergic receptor, were unaffected in Vps37aKD livers (Figures S3B and S3C). In fact, activation of this receptor by isoproterenol had no effect on p-PKA substrates upon Vps37a depletion in primary hepatocytes (Figures S3D and S3E), demonstrating a preferential function of Vps37a in Gcgr signaling.

To assess whether the observed increase in glucose production upon Vps37aKD was also dependent on Gcgr *in vivo*, we utilized a Gcgr antagonist IUB396 (Yang et al., 2021). Confirming its inhibitory function, IUB396 repressed glucagon-induced p-Creb activation in primary mouse hepatocytes (Figures S3F and S3G). Interestingly, acute intra-peritoneal injection of IUB396 prior to pyruvate stimulation completely blocked the increase in HGP upon reduction of Vps37a (Figures 3D and 3E), supporting the notion that the metabolic effects of Vps37aKD occur through Gcgr.

To further confirm the role of Vps37a in glucagon signaling, we pioneered overexpressing (OE) Vps37a in mouse livers for 7 weeks using an AAV8-LP1-mVps37a expression construct and observed a 60% increase in Vps37a protein levels (Figures 3F and 3G). Interestingly, this elevation let to increased protein levels of ESCRT-I components Tsg101, Vps28, and Vps37c by 40%, 100%, and 30%, respectively, without changing Vps37b levels, indicating a general increase in abundance of this complex (Figures 3F and 3G). The induction of ESCRT-I decreased p-PKA substrates, p/t-Creb and cAMP levels (Figures 3H–3J), suggesting lower cAMP/PKA/p-Creb activation. Indeed, this reduction increased glycogen levels (Figure 3K) and decreased fasting blood glucose concentrations (Figure 3L) without affecting TG content (Figure 3M), further supporting a regulatory role for Vps37a in glucagon signaling.

However, the reduction of cAMP and blood glucose levels was dependent on the magnitude of Vps37a OE. A 30% increase of Vps37a protein levels in an independent cohort was insufficient to enhance ESCRT-I protein abundance (Figures S3H and S3I), correlating with no effect on cAMP activation (Figure S3J) and alterations in blood glucose levels (124.6 versus 124.5 mg/dL of control versus Vps37a OE). These data are consistent with an intrinsic auto-regulatory posttranslational regulation of the protein abundance of ESCRT-I in OE studies (Feng et al., 2000), indicating that the protein levels of Vps37a and ESCRT-I are tightly regulated and that the beneficial effects on lowering blood glucose potentially require the collective function of the entire complex. Altogether, these data strongly suggest a unique role of Vps37a and ESCRT-I in the regulation of glucagon signaling-controlled glucose metabolism in the liver.

Reduction of Vps37a causes hyperglycemia and insulin resistance in mice fed a high-fat diet

As overactivation of HGP is a hallmark of T2D, we tested whether the stimulatory effects on glucose output under Vps37aKD would manifest into a metabolically impaired condition. Thus, we down-regulated Vps37a through bi-weekly injections of LNPs in mice fed a 60% high-fat diet (HFD) and observed an 80% reduction

(C–E) (C) Relative expression of *G6pc* and *Pck1* in isolated hepatocytes from hetero- and homozygous $Gcgr^{-/-(liver)}$ KO mice (n = 3). ipPTT in wild-type mice pretreated without (n = 6) (D) or with (n = 5) IUB396 (E).
(F and G) (F) Representative western blots for Vps37a, Vps37b, Vps37c, Vps28, and Tsg101 in livers from CTR or OE mice with quantifications in (G).
(H and I) (H) Representative western blots of p-PKA substrates, p- and t-Creb, and quantifications in (I).
(J–M) cAMP (J) and glycogen content (K), blood glucose levels (L), and liver TG content (M) (n = 6).
All animals for OE experiments were treated with control (CTR) or Vps37a-overexpressing (OE) AAVs. Primary hepatocytes treated with control (CTR) or Vps37a (KD) siRNA (mean ± SEM). *p < 0.05, **p < 0.01, ***p < 0.001, and ****p < 0.0001 by two-tailed unpaired Student's t test.

CellPress
OPEN ACCESS

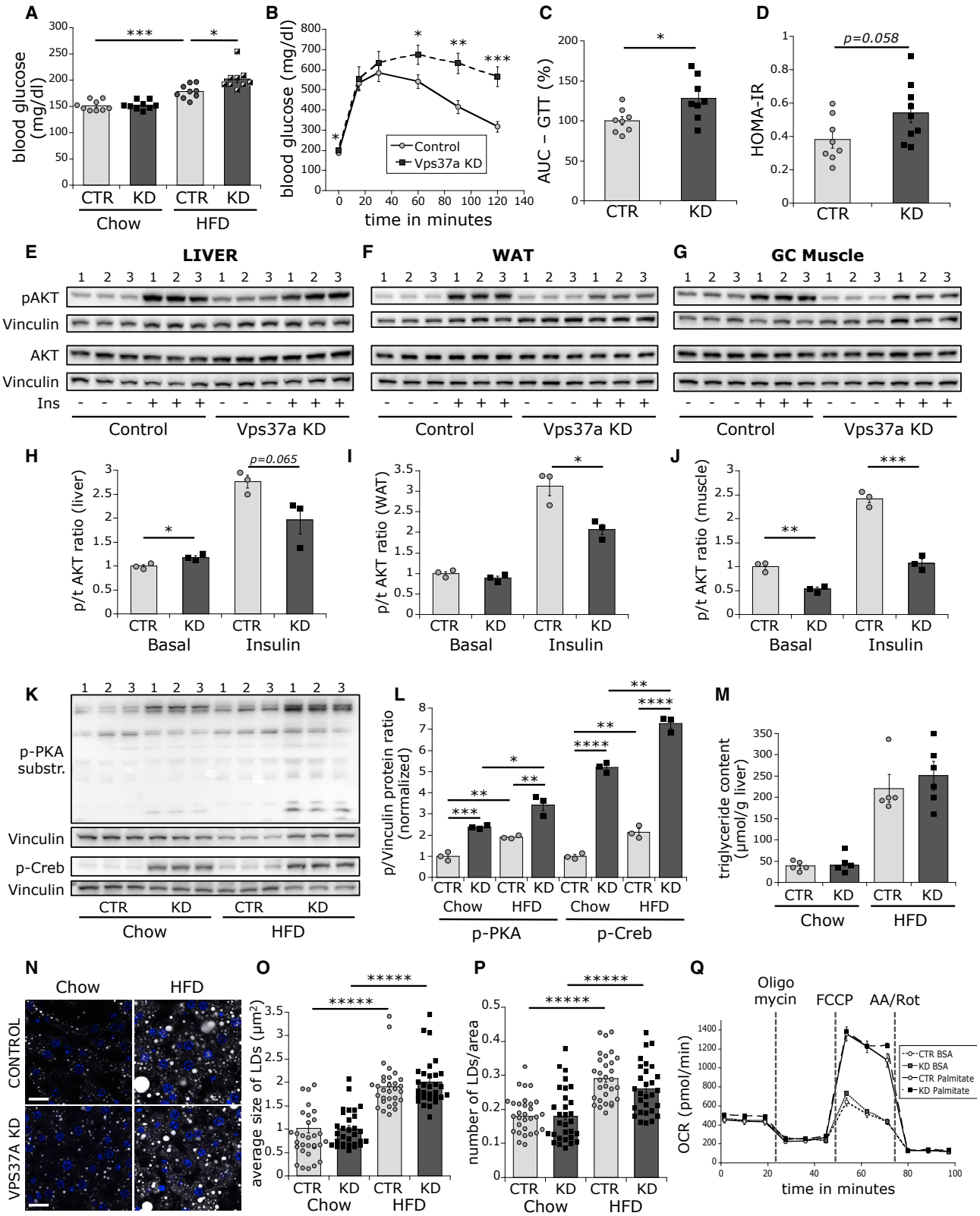

Figure 4. Vps37aKD in HFD mice induces hyperglycemia without changing lipid metabolism

(A) Fed blood glucose levels in chow or HFD mice.

(B–D) ipGTT (B), area under the curve of the GTT (C), and HOMA-IR levels (D) (n = 8–9).

(legend continued on next page)

of Vps37a protein levels without affecting body weight gain (Figures S4A–S4C). Interestingly, at 13 weeks of HFD, Vps37a-depleted mice developed enhanced hyperglycemia (Figure 4A) without affecting serum insulin levels (Figure S4D), suggesting that the stimulatory effect on HGP under Vps37aKD led to a further imbalance in glucose homeostasis. Indeed, HFD-fed Vps37aKD mice showed a worse glucose intolerance than controls (Figure 4B), along with higher AUC (Figure 4C) and increased homeostatic model assessment of IR (HOMA-IR) levels (Figure 4D).

To understand whether the effect of Vps37aKD on glucose homeostasis was associated with decreased insulin sensitivity, we checked p-AKT activation in liver, muscle, and adipose tissue upon insulin injection. Indeed, prolonged reduction of Vps37a under HFD caused reduced insulin-induced p-AKT activation, indicating induction of liver and peripheral IR (Figures 4E–4J), which is in agreement with previous reports on the development of IR after sustained activation of liver p-Creb signaling (Hogan et al., 2015). Consistent with the effects of Vps37aKD in wild-type mice, we observed increased abundance of p-PKA substrates and p-Creb (Figures 4K and 4L) in control and Vps37a-depleted chow- and HFD-fed mice, as well as elevated nuclear localization of p-Creb (Figures S4E–S4G). Indeed, activation of Creb resulted in higher expression of *G6pc* and *Pck1* (Figure S4H), without alteration of *Gcgr*, *Foxo1*, or *Creb*. Depletion of Vps37a in HFD-fed mice induces hyperglycemia and deteriorates glucose tolerance by overactivating hepatic PKA/Creb signaling, thus highlighting the contribution of Vps37a to the maintenance of glucose homeostasis in HFD-fed mice.

Lipid metabolism is unaltered upon Vps37a KD

Gcgr signaling induces β-oxidation at the same time as activating gluconeogenesis (Galsgaard et al., 2019; Perry et al., 2020). Our data showing a selective increase in signaling via the cAMP/PKA/p-Creb pathway to glucose metabolism, but not to AMPK, and CaMKII suggest an uncoupling of this connection. Thus, we wondered whether Vps37a affected lipid metabolism upon HFD. Strikingly, we found no difference in liver TG content between control and Vps37aKD chow- or HFD-fed mice (Figure 4M), which was further confirmed by Bodipy staining showing no differences in lipid droplet (LD) size or number (Figures 4N–4P) and histology of lipid accumulations in HFD livers (Figures S4I and S4J). In addition, no alterations in serum TGs, low-density lipoprotein (LDL), ALT, or AST levels were observed, indicating intact lipid metabolism and no detrimental effects on liver health in Vps37a KD mice (Table S4).

Liver lipid content is dependent on the uptake, utilization, and secretion of lipids. To address these options, we measured LDL internalization into primary hepatocytes over a 45-min period and saw no difference, indicating similar uptake capacities (Figure S4K). To test whether KD of Vps37a altered lipid usage, we assessed the oxygen consumption rate (OCR) upon palmitate treatment as a measure of fatty acid β-oxidation. The increase in OCR upon palmitate treatment was not further enhanced by Vps37aKD (Figure 4Q), indicating no effect on lipid breakdown. Although we observed a small elevation in the basal respiration upon palmitate addition in Vps37aKD cells, ATP production and maximal respiration were unchanged (Figure S4L), confirming the unaltered LD size and number in livers from HFD-fed mice. Moreover, mRNA and protein levels of fatty acid synthase (Fas) and Acc and the expression of *Cd36*, *Dgat2*, or *Cpt1α* were unchanged in Vps37a-depleted HFD-fed mice (Figures S4M–S4O), indicating similar lipid usage. Finally, we examined lipid secretion *in vitro* using a cholesterol secretion assay and TG production *in vivo* after Tyloxapol injections and found no difference upon Vps37a reduction (Figures S4P and S4Q). Thus, depletion of Vps37a has no influence on lipid metabolism at the level of lipid uptake, signaling, accumulation, breakdown, and secretion under basal condition.

To address whether Vps37a reduction affected glucagon-stimulated lipid accumulation, we measured LDs in primary hepatocytes treated with fatty acids or BSA for 24 h with or without glucagon treatment (Figures S4R–S4T). Glucagon caused a decrease in the size of LDs while increasing their number, suggesting a shift toward droplet usage (Galsgaard et al., 2019). Importantly, Vps37aKD had no effect on basal or glucagon-stimulated LD formation and usage (Figures S4R–S4T), clearly supporting a specific role for Vps37a in glucose production.

As *VPS37A* expression was reduced in patients with obesity and T2D and OE Vps37a had the potential to lower blood glucose levels, we wondered whether OE of Vps37a in a diabetic mouse model could have a beneficial effect on reducing hyperglycemia. Consistent with the results from the patients with T2D, we found Vps37a protein levels to be reduced by 30% in diabetic *db/db* mice compared with heterozygous controls (Figures S3K and S3L). Interestingly, OE of Vps37a in 7-week-old *db/db* mice for 5 weeks induced a 70% increase in Vps37a protein levels, which was associated with a 50% reduction in cAMP in the liver and decreased p-PKA substrate and p-Creb (Figures S3M–S3O). These reductions in cAMP signaling were accompanied by a tendency for lower blood glucose levels without changing liver TG content (Figures S3P and S3Q). These data suggest that increasing Vps37a could be beneficial for altering hepatic glucagon signaling toward decreasing hyperglycemia under diabetic conditions.

The induction of p-Creb signaling to gluconeogenesis is specific to Vps37a

Vps37a, as member of ESCRT-I, is involved in directing ubiquitinated membrane receptors to lysosomes for degradation (Stuffers et al., 2009). This role requires the functional integrity

(E–J) Representative western blots for liver p-and t-Akt (E), WAT (F), and muscle (G) of insulin-injected HFD mice and quantification in (H)–(J).
(K and L) (K) Representative western blots for p-PKA substrates in liver of chow and HFD mice, quantified in (L).
(M) TG content in chow and HFD livers (n = 5–6 per condition).
(N–P) (N) Representative single confocal liver slices of chow and HFD mice labeled with Bodipy (gray) and DAPI (blue) and quantification of LD size (O) and number (P) (n = 25–30). Scale bars, 20 μm.
(Q) Seahorse OCR measurements ± palmitate treatment in primary hepatocytes (n = 10 wells).
All animals treated with control (CTR) and Vps37a (KD) LNPs for 13 weeks with bi-weekly injection. Primary hepatocytes treated with control (CTR) or Vps37a (KD) siRNA (mean ± SEM). *p < 0.05, **p < 0.01, ***p < 0.001, ****p < 0.0001, and *****p < 0.00001 by two-tailed unpaired Student's t test.

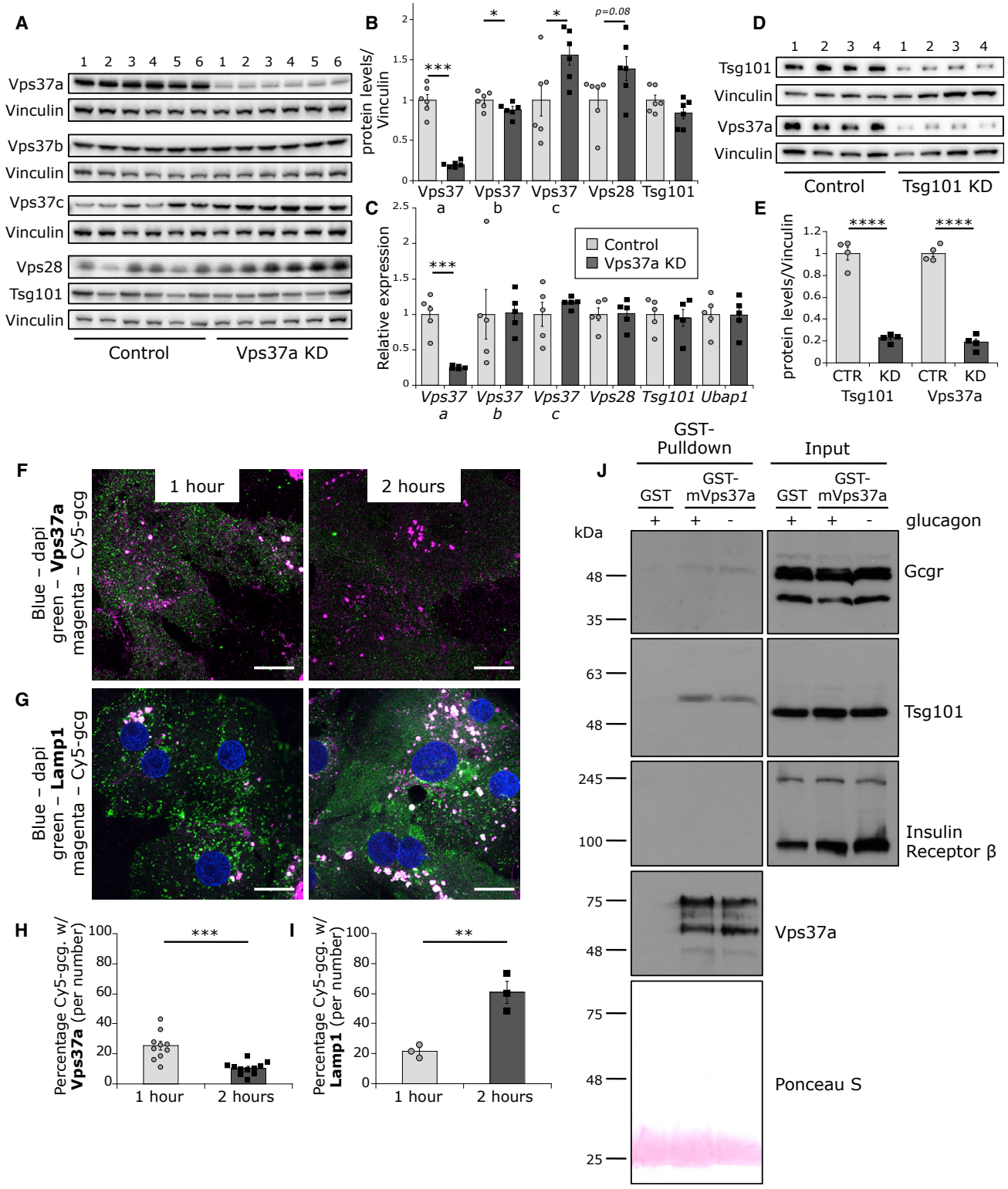

Figure 5. Vps37a interacts with Gcgr

(A and B) (A) Representative western blots of liver Vps37a, Vps37b, Vps37c, Vps28, and Tsg101 protein and quantifications in (B) (n = 6).

(C) Relative mRNA of *Tsg101*, *Vps37a*, Vps37b, Vps37c, *Vps28*, and *Ubap1 in vitro* (n = 5).

(D and E) (D) Representative western blots of Vps37a and Tsg101 upon Tsg101KD in hepatocytes, quantified in (E).

(F–I) Representative single confocal slices of Cy5-glucagon uptake for 1 and 2 h in primary human hepatocytes stained for Vps37a (n = 10–11) (F), Lamp1 (n = 3) (G), and quantification using particle analysis in (H) and (I). Scale bars, 20 μm.

(legend continued on next page)

of the entire complex. To test whether the effects of Vps37aKD are mediated by destabilizing ESCRT-I, we measured the abundance of the other complex members. Interestingly, Vps37aKD induced Vps37c protein levels by 50%, whereas Vps37b was slightly decreased, indicating a counter regulation of the Vps37 isoforms. There was a tendency of increased protein abundance for Vps28 and no effect on Tsg101, indicating intact ESCRT-I stability upon Vps37aKD, as reported before (Kolmus et al., 2021). The observed changes were due to protein turnover, as mRNA levels of all ESCRT-I members were unaffected (Figures 5A–5C). In contrast, KD of Tsg101 caused a reduction in Vps37a protein levels (Figures 5D and 5E), consistent with previous data (Bache et al., 2004), without decreasing ESCRT-I gene expression (Figure S5A). These data suggest that the observed metabolic effects of Vps37a are independent of ESCRT-I stability.

As there were some counter regulations of the other components of ESCRT-I upon Vps37aKD and OE, we wondered whether the effects on p-Creb activation and gluconeogenic gene induction are specific to Vps37a. To test this, we downregulated Tsg101, Vps28, Vps37b, and Vps37c individually in primary hepatocytes and measured basal and glucagon-induced p-Creb and concomitant induction in *G6pc* and *Pck1* gene expressions (Figures S5B–S5G). Importantly, when depleted, none of the other ESCRT-I component mimicked the Vps37a phenotype of inducing p-Creb and gluconeogenic genes in basal and glucagon-stimulated states. There was a marginal increase in *G6pc* and *Pck1* genes under Vps37cKD upon glucagon stimulation (Figure S5G) and a decrease in basal and glucagon *Pck1* levels under Vps28 and Vps37bKD, respectively (Figures S5E and S5F). However, KD of none of the other subunits of ESCRT-I affected p-Creb activation (Figures S5B and S5C), indicating that the observed stimulation of the PKA/Creb pathway is mediated via Vps37a.

To address whether reducing Vps37a levels had any consequence for endo-lysosomal compartments, we stained early endosomes with early endosomal antigen 1 (Eea1) and late endosomes and lysosomes with lysosomal-associated membrane protein 1 (Lamp1). Interestingly, Vps37aKD resulted in a significant accumulation of Eea1 and a reduction of Lamp1 fluorescence intensity (Figures S5H and S5J), hinting at an accumulation of early endosomes and less abundance of Lamp1-positive lysosomes. These data indicate alterations in early-to-late endosomal progression in primary hepatocytes, which was reported for EGFR trafficking in HeLa cells (Bache et al., 2004). Indeed, Vps37a depletion caused a 30% intracellular accumulation of fluorescently labeled EGF, indicating less degradation (Figures S5I and S5K), although the magnitude of the effect was less pronounced compared with HeLa cells (Bache et al., 2004).

Vps37a controls trafficking of Gcgr through endosomes

Since Vps37a seems to regulate early-to-late endosomal transport and its metabolic effects are Gcgr dependent, we hypothesized that Vps37a plays a role in Gcgr trafficking and signaling. To study the intracellular distribution and trafficking of Gcgr, we developed a fluorescent Cy5-glucagon agonist, since the currently available Gcgr antibodies are not usable for trafficking studies (Bomholt et al., 2021). This allowed us to follow endogenous surface and internalized Gcgr with Cy5-glucagon, as shown before for other labeled agonists (Abdullah et al., 2016; Ansarullah et al., 2021; Godbole et al., 2017). To address its functionality, we first tested how efficiently Cy5-glucagon could activate Gcgr signaling. As expected for a labeled agonist, activation of p-Creb required 2.5× higher concentrations of Cy5-glucagon relative to unlabeled ligand (Figures S6A and S6B). In addition, binding to Gcgr was confirmed by competition experiments, in which 20-fold excess unlabeled glucagon suppressed the Cy5 signal by 50% (Figures S6C and S6D), indicating its utility as a readout for Gcgr trafficking by fluorescence microscopy in primary hepatocytes.

To investigate whether Vps37a is involved in Gcgr trafficking, we analyzed colocalization of VPS37A with Cy5-glucagon in primary human hepatocytes over time. Interestingly, internalization of Cy5-glucagon for 1 h resulted in a 25% colocalization of labeled glucagon with VPS37A, which decreased after 2 h (Figures 5F and 5H). This decrease was associated with an increase in its abundance in lysosomes of up to 60% based on colocalization with LAMP1 (Figures 5G and 5I), pointing to its enhanced degradation at later time points.

To check whether Vps37a truly interacted with Gcgr, we performed pull-down experiments with purified glucagon stimulation test (GST)-tagged Vps37a or GST alone (Figures S6E and S6F) from whole liver lysates of phosphate-buffered saline (PBS) or glucagon-injected mice. As a positive control, GST-bound Vps37a was able to pull-down Tsg101 from both lysates, confirming binding specificity. Strikingly, we found a specific interaction of Vps37a with Gcgr but not with Insr under basal and glucagon-stimulated conditions (Figure 5J), highlighting specificity of Vps37a to Gcgr (Figures S3B–S3E). Altogether, these data strongly support a role of Vps37a in mediating Gcgr trafficking by interacting with the receptor.

Vps37a has a putative ubiquitin-binding domain (Stuffers et al., 2009); however, direct ubiquitinated cargoes have not been discovered so far. To check whether GCGR undergoes ubiquitination-mediated internalization, we performed high-resolution microcopy in primary human hepatocytes. Indeed, colocalization analysis revealed 13% colocalization of GCGR with pan-ubiquitin in small puncta structures in the basal state, which increased with glucagon to 17%, suggesting that a fraction of GCGR is ubiquitinated for potential degradation (Figures S6G and S6H). Whether this ubiquitination signal is directly attached to the receptor or an adaptor, such as β-arrestin, as shown for other GPCRs (Marchese and Trejo, 2013) and whether receptor degradation increases with longer stimulations, as suggested previously (Authier and Desbuquois, 2008; Krilov et al., 2008), need to be elucidated in further studies.

(J) Pull-down for Gcgr, Tsg101, and Insr-β from liver lysates from PBS and glucagon-injected mice incubated with recombinant GST-mVPS37A or GST control, analyzed by immunoblotting. Presence of GST was detected by Ponceau S.

All animals and hepatocytes treated with control (CTR) and Vps37a (KD) LNPs or siRNA (mean ± SEM). *p < 0.05, **p < 0.01, ***p < 0.001, and ****p < 0.0001 by two-tailed unpaired Student's t test.

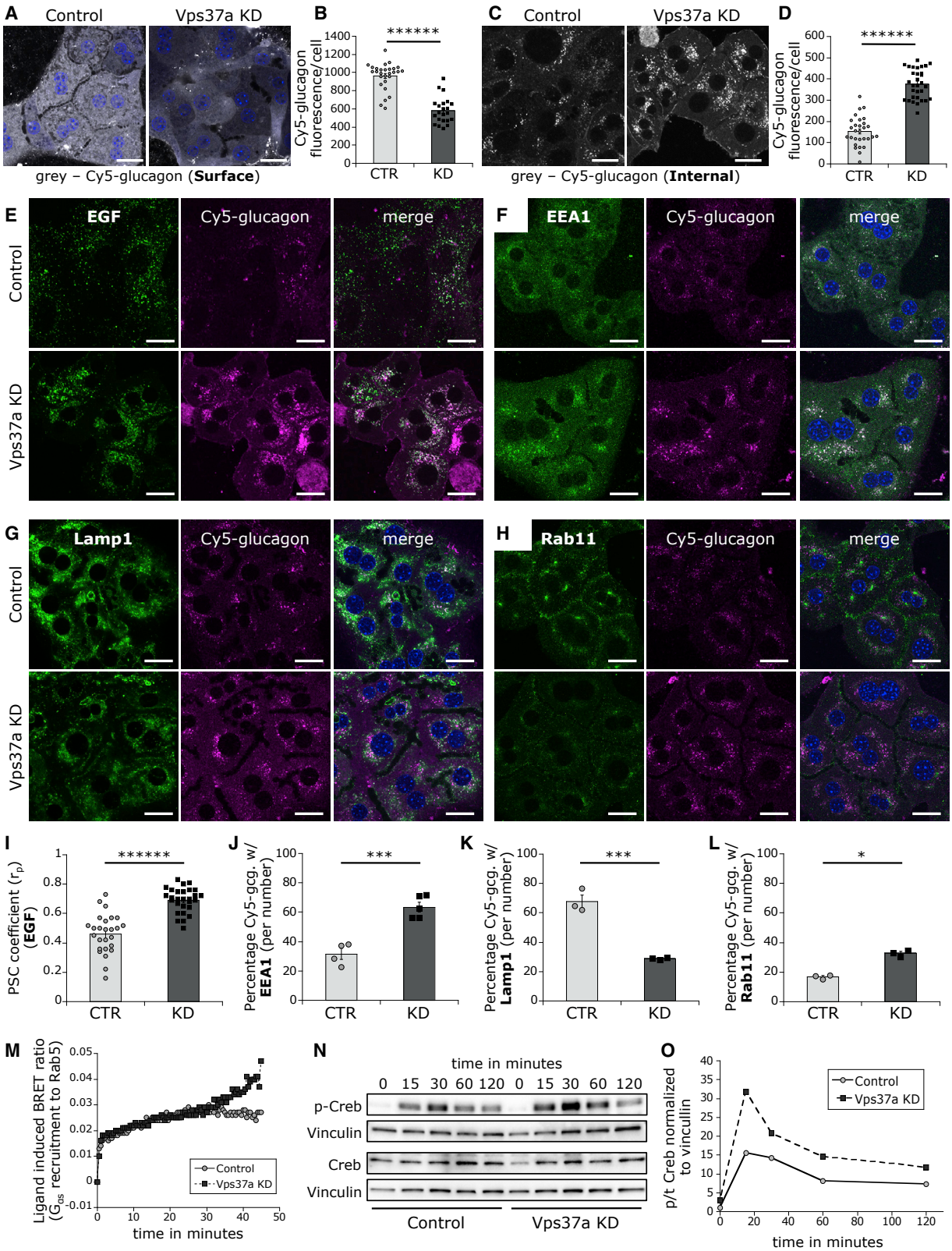

(legend on next page)

Vps37a KD causes accumulation of Gcgr in endosomes

To test whether the loss of Vps37a had any effect on the intracellular distribution of Gcgr labeled by Cy5-glucagon, we measured the surface and internal pool of Gcgr upon Vps37aKD. Remarkably, KD of Vps37a reduced PM Gcgr levels by 40%, as measured by Cy5-glucagon binding on ice (Figures 6A and 6B) and increased the intracellular pool 3-fold, based on continuous uptake of Cy5-glucagon over 6 h (Figures 6C and 6D). Thus, Vps37a depletion shifts receptor localization to intracellular compartments. To examine their identity, we analyzed colocalization of Cy5-glucagon with internalized EGF, Eea1, Lamp1, and the recycling endosomal marker Rab11 (Figures 6E–6H). Intriguingly, Vps37a KD caused 40% and 50% increases in the colocalization with EGF and Eea1, respectively (Figures 6I and 6J), whereas its colocalization with Lamp1 decreased by 60% (Figure 6K), consistent with enhanced endosomal and reduced lysosomal localization. Surprisingly, we observed reduced numbers of Rab11-positive recycling endosomes under Vps37aKD (Figure 6H), which was associated with a 10% increase in colocalization with Cy5-glucagon. These data suggest an additional accumulation of Gcgr in Rab11-positive endosomes upon Vps37aKD (Figure 6L), which could contribute to the reduced surface expression of the receptor. Altogether, this points toward delayed Gcgr trafficking to lysosomes upon Vps37aKD, leading to its enhanced abundance in early and partially recycling endosomes.

Endosomal localization of class A GPCRs can sustain cAMP/PKA signaling to activate downstream nuclear targets (Eichel and von Zastrow, 2018; Ferrandon et al., 2009; O'Banion et al., 2019; Vilardaga et al., 2014). Thus, the endosomal accumulation of Gcgr could be responsible for the overactivation of glucagon signaling under Vps37a depletion. To address this, we measured the degree of active ligand-bound receptor within Rab5-positive endosomes using mini-$G_{\alpha s}$ and observed an elevated time-dependent accumulation of endosomal $G_{\alpha s}$ upon VPS37AKD, indicating increased abundance of ligand-bound GCGR in endosomes (Figure 6M). Given the role of VPS37A in trafficking endosomal cargo to lysosomes, these data indicate that the enhancement on GTP-$G_{\alpha s}$ formation (Figure 1R) is derived from prolonged localization of ligand-bound GCGR within Rab5-endosomes. Consequently, delay in degrading the receptor would slow down clearance of glucagon-induced p-Creb activation. To test this, we pulsed cells with glucagon and measured the appearance of p-Creb over the following chase period. p-Creb stimulation peaked 15–30 min after the glucagon pulse in control cells and declined back to almost basal levels by 120 min. Vps37aKD cells exhibited a higher peak of p-Creb, as observed before, but also maintained higher phosphorylation of Creb throughout the chase period (Figures 6N and 6O), showing an increase in the magnitude and duration of Gcgr activation of p-Creb. Altogether, these data strengthen a regulatory role of Vps37a in Gcgr trafficking, where its loss causes an accumulation of the receptor in endosomes. The increase in endosomal Gcgr was associated with activation of cAMP/PKA-mediated Creb phosphorylation and induction of gluconeogenic genes, without affecting lipid metabolism, suggesting that internalized Gcgr in endosomes continues to signal only to glucose metabolism.

Endosomal localization of Gcgr is required for cAMP/PKA/p-Creb-mediated activation of gluconeogenesis

If endosomal localization is indeed responsible for differential signaling from Gcgr to the gluconeogenic pathway, redirecting the receptor back to the PM should block this activation. Gcgr interacts with β-arrestin-2 on the PM, thereby inducing its internalization upon glucagon stimulation (Zhu et al., 2017) and KD of β-arrestin-2, but not β-arrestin-1, in the liver blocks receptor internalization causing its redistribution to the PM (Zhu et al., 2017). Analysis of the effect of β-arrestin-2 depletion in primary hepatocytes revealed enhanced binding of Cy5-glucagon to the receptor at the PM (Figures S7A and S7B) without significantly affecting β-arrestin-1 expression (Figure S7C). However, no basal activation of p-Creb and no induction of gluconeogenic genes were observed (Figures S7C and S7D), indicating that PM-localized Gcgr does not induce basal stimulation of the cAMP/PKA/p-Creb pathway per se but requires glucagon binding for activation (Zhu et al., 2017).

To determine whether endosomal localization is responsible for basal cAMP/PKA/p-Creb signaling, we performed side-by-side KD experiments of Vps37a, β-arrestin-2, and double KD (DKD). As shown before, KD of Vps37a reduced surface expression of Gcgr, whereas β-arrestin-2 depletion enhanced its PM localization (Figures 7A and 7B). As anticipated, DKD of Vps37a and β-arrestin-2 redirected the receptor to the cell surface (Figures 7A and 7B), which was associated with a loss of the stimulatory effect of Vps37aKD on p-PKA and p-Creb (Figures 7C–7E) and induction in gluconeogenic genes in the basal state (Figures 7F and 7G). Thus, these data provide evidence that endosomal localization of Gcgr is capable of activating the cAMP/PKA/p-Creb pathway even without ligand binding, as shown for other GPCRs (Gilliland et al., 2013; Irannejad et al., 2013; Scarselli and Donaldson, 2009).

As PM-localized Gcgr under β-arrestin-2 KD activates both gluconeogenesis and lipid breakdown upon glucagon stimulation (Zhu et al., 2017), we wondered whether redirected Gcgr

Figure 6. Vps37aKD causes an accumulation of Gcgr in endosomes

(A and B) (A) Representative single confocal slices of hepatocytes incubated for 2 h on ice with Cy5-glucagon and quantification in (B) (n = 22–28).

(C and D) (C) Representative confocal hepatocyte images (max. projections of 2 middle slices) incubated for 6 h with Cy5-glucagon for internal Gcgr and quantification in (D) (n = 31).

(E and I) (E) Colocalization analysis (max. projections of 3 middle slices) of Cy5-glucagon and alexa555-EGF co-internalized (6 h) and quantification in (I) (n = 26–28).

(F–H and J–L) Representative single confocal slices of Cy5-glucagon (2 h) co-stained with EEA1 (n = 4–5) (F), Lamp1 (n = 3) (G), Rab11 (n = 3) (H), and quantification using particle analysis (J–L). Scale bars, 20 μm.

(M) Temporal resolution of ligand-induced mini-$G\alpha_s$-Nluc recruitment to untagged Gcgr in Venus-Rab5 positive endosomes in HEK cells.

(N and O) Representative western blot of p-Creb activation over time after an initial glucagon pulse, chased in normal medium and quantification in (O).

Primary hepatocytes treated with control (CTR) or Vps37a (KD) siRNA (mean ± SEM). *$p < 0.05$, ***$p < 0.001$, and ******$p < 0.000001$ by two-tailed unpaired Student's t test.

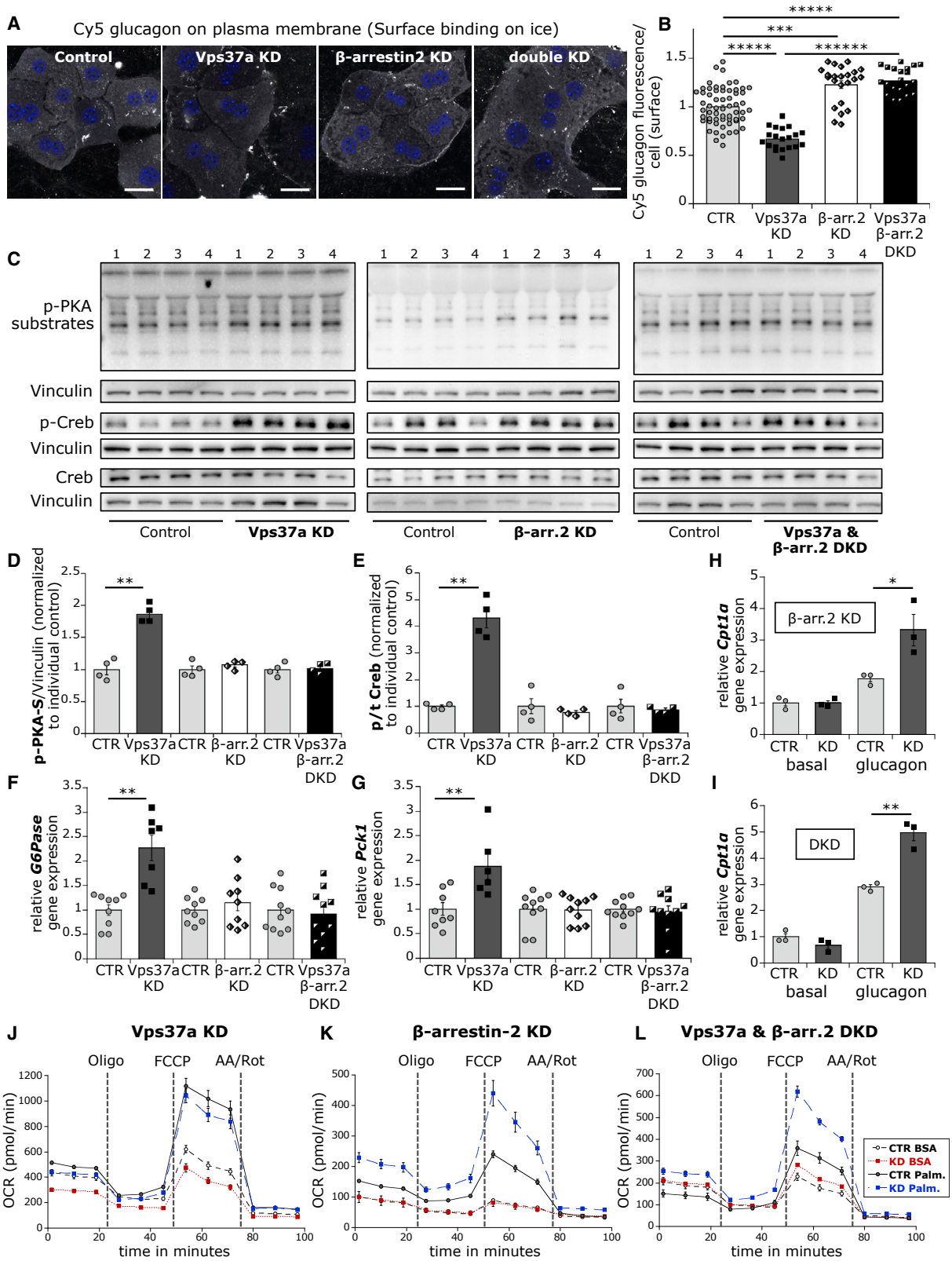

Figure 7. DKD of Vps37a and β-arrestin-2 shifts glucagon receptor back to the PM and inactivates p-PKA/Creb signaling

(A and B) (A) Representative confocal hepatocyte images (max. projections of two middle slices) upon control, Vps37a, β-arrestin-2, and DKD incubated for 2 h on ice with Cy5-glucagon and quantification in (B) (n = 20–60).

(legend continued on next page)

under DKD would now lose the signaling preference to glucose metabolism. Therefore, we stimulated primary hepatocytes with glucagon and measured the effect on p-Creb activation, gene expression, and β-oxidation upon Vps37a, β-arrestin-2, and DKD. Glucagon increased p-Creb levels (Figures 7F, 7G, S7E, and S7F) as well as the expression of *G6pc* and *Pck1* (Figures 7H, 7I, S7G, and S7H) under all conditions. Interestingly, we found a glucagon-stimulated upregulation of *Cpt1a* expression (Figures 7H and 7I) as well as an induction in β-oxidation with increased OCR (Figures 7J–7L and S7I–S7K) in β-arrestin-2 and DKD but not in Vps37aKD cells, indicating enhanced mitochondrial lipid transport and usage. Thus, elevated PM localization of Gcgr by β-arrestin-2 KD further activates lipid breakdown upon glucagon stimulation. Altogether, these data show that endosomal localization of the Gcgr induced by Vps37aKD is responsible for the preferential increased glucagon signaling to glucose but not to lipid metabolism. Thus, uncoupling of glucose production from β-oxidation downstream of Gcgr signaling is dependent on its endosomal localization.

DISCUSSION

Here, we demonstrate that Gcgr signaling-mediated regulation of HGP can be controlled independently of its role in lipid metabolism by altering the intracellular distribution of Gcgr. KD of the endosomal protein Vps37a shifts Gcgr localization to endosomes, generating a sustained and specific overactivation of the cAMP/PKA/Creb pathway in basal state that causes enhanced glucose output without affecting lipid usage. When the receptor is redirected to the PM, glucagon once again activates β-oxidation along with gluconeogenesis. Thus, endosomal localization of Gcgr uncouples glucose from lipid metabolism downstream of Gcgr signaling.

Our data reveal how controlling Gcgr intracellular localization leads to alterations in glucagon signaling with physiological impact on HGP. Like all transmembrane receptors, Gcgr undergoes constitutive endocytosis also in the basal state due to reorganization of the PM. Thus, Gcgr is internalized even without ligands, as shown for other RTKs and GPCRs (Seifert and Wenzel-Seifert, 2002; Sutkeviciute and Vilardaga, 2020). However, its particular path and kinetics through the endosomal system are not known. Using a Cy5-glucagon agonist, we show that reduction of Vps37a decreases the PM localization of Gcgr and increases the receptor localization to endosomes. This is most likely not due to a direct facilitation of receptor internalization, as ESCRT-I proteins are not involved in transport from the PM but rather due to an effect of Vps37a on Gcgr trafficking through endosomes. In fact, blocking endocytosis *in vitro* by dynamin inhibitors revealed a contribution of endosomal signaling of Gcgr to gluconeogenic gene expression (Cajulao et al., 2022). However, redistributing Gcgr through other means than interfering with Vps37a, such as overexpression of RAMP2 had no effect on gluconeogenesis or signaling *in vivo* (McGlone et al., 2021). This points toward a specific regulatory role of ESCRT-I-positive endosomes in determining Gcgr signaling and regulation of glucose metabolism. As the regulation on glucagon signaling to cAMP/PKA/Creb pathway are specific for Vps37a and not phenocopied by depletion of other ESCRT-I members, they support a unique role of Vps37a in Gcgr trafficking and signaling, further substantiated by the observed interaction of Vps37a with Gcgr. However, a stable ESCRT-I complex is required for the trafficking function of Vps37a. Indeed, we observed that OE Vps37a increased the protein abundance of other ESCRT-I members, which is consistent with previous studies on ESCRT-I stability and function (McDonald and Martin-Serrano, 2008). Thus, endosomal trafficking via a Vps37a-containing ESCRT-I complex adds an additional layer of potential regulation in Gcgr signaling with consequences for systemic metabolic homeostasis.

Our results raise the question of how changing Gcgr localization preferentially activates gluconeogenesis, since we observed no changes in TG content or in basal and glucagon-stimulated β-oxidation, which is different from the observations made in β-arrestin-2 KD mice (Zhu et al., 2017). β-arrestin-2 depletion causes enhanced Gcgr localization to the PM, whereas Vps37aKD increases the presence of the receptor in endosomes. In fact, sustained $G_{\alpha s}$-protein signaling to the cAMP/PKA/Creb pathway has been reported on endosomes through the formation of multi- or mega-plexes between GPCR, β-arrestin-2, and G-proteins (Clark et al., 2020; Thomsen et al., 2016). Thus, the endosomal Gcgr population will facilitate sustained $G_{\alpha s}$-protein signaling, supported by prolonged p-Creb activation in hepatocytes. However, $G_{\alpha q}$ signaling, responsible for activating β-oxidation from the PM through IP_3 formation (Perry et al., 2020), has so far not been reported to occur from intracellular organelles (Sutkeviciute and Vilardaga, 2020). The differences in these signaling mechanisms can be explained by the different membrane properties and curvatures, as the PM is a relatively even surface (Harayama and Riezman, 2018), whereas the endosomal membrane has a high curvature and a different lipid composition, which could lead to distinct recruitment of signaling effectors (Sutkeviciute and Vilardaga, 2020). The fact that we can rescue glucagon-induced β-oxidation by arresting the receptor at the PM in Vps37a/β-arrestin-2 DKD supports this hypothesis, since these changes in localization would be associated with distinct membrane compositions and properties.

Our finding that simply changing the localization of a GPCR alters its basal signaling activity suggests that the environment on the endosomal membrane favors a constitutively active confirmation of Gcgr, as has been observed previously (Hjorth et al., 1998; Seifert and Wenzel-Seifert, 2002). Indeed, the high curvature of the endosomes could initiate a twist of the transmembrane region of Gcgr, thereby exposing the binding pocket of

(C–G) (C) Representative western blots and their quantification for basal p-PKA substrates (D) and p-Creb (E) (n = 4) and relative mRNA of *G6Pase* (F) and *Pck1* (G) in primary hepatocytes upon control, Vps37a, β-arrestin-2, and DKD (n = 6–10).
(H and I) *Cpt1α* expression upon glucagon stimulations under β-arrestin-2 and DKD (n = 3).
(J–L) Seahorse OCR ± palmitate treatment upon 24 h glucagon stimulations (n = 5 wells).
Primary hepatocytes treated with control (CTR), Vps37a, β-arrestin-2, and double (KD) siRNA (mean ± SEM). **p < 0.01, ***p < 0.001, ****p < 0.0001, and *****p < 0.00001 by two-tailed unpaired Student's t test.

G-proteins for interactions on endosomes (Mattedi et al., 2020). As all GPCRs go through a basal activity state that sets the threshold for ligand activation (Weis and Kobilka, 2018), prolonging the presence in endosomes would stabilize this basal activity, leading to sustained signaling. To understand why this is specific for $G_{\alpha s}$ and not $G_{\alpha q}$ signaling will require *in vitro* reconstitution assays of purified Gcgr within different cellular membranes, where specific G-protein coupling is measured, as performed for some class A GPCRs (Yen et al., 2018). Indeed, we found enhanced ligand-induced $G_{\alpha s}$ recruitment to Rab5-positive endosomes upon VPS37AKD, confirming sustained endosomal $G_{\alpha s}$ signaling for the GCGR. However, further work is needed to understand how different cellular membranes influence the structure-activity relationship of Gcgr under basal and glucagon conditions.

The fact that overactivation of Gcgr signaling to glucose metabolism from endosomes manifests as hyperglycemia and IR under HFD clearly supports a significant contribution of endosomal signaling through Gcgr for metabolic diseases. The strong reduction of *VPS37A* expression in patients with T2D and obesity suggests a potential dysregulation of intracellular trafficking of GCGR in metabolic disorders. In fact, alterations in membrane transport have been observed in HFD-fed mice (Krahmer et al., 2018) and patients with NAFLD (Seitz et al., 2019), potentially contributing to disease manifestation. Thus, interfering with intracellular trafficking and receptor localization could be a strategy to uncouple Gcgr signaling and overcome the problems associated with targeting Gcgr in diabetes.

Limitations of study

Our current study identified a physiological role of Vps37a and ESCRT-I in modulating Gcgr signaling in the liver with the potential to reduce circulating blood glucose levels without affecting fatty acid oxidation. We found *VPS37A* to be downregulated in patients with obesity and T2D, which could contribute to their disease condition. However, our study does not address cause and consequence of this reduction. Although reintroducing Vps37a had the potential to reduce circulating glucose levels, it required the collective function of the entire ESCRT-I complex. This suggests a more complicated contribution of ESCRT-I to metabolic homeostasis. We still know too little about the different ESCRT-I subcomplexes in different tissues and how they affect complex assembly and function in physiological and disease condition (Kolmus et al., 2021; Okumura et al., 2013). Thus, more work is required to understand how ESCRT-I components are transcriptionally regulated, stabilized, or activated to target this pathway in T2D. In addition, future studies are needed to dissect how intracellular trafficking of Gcgr is regulated, beyond the role of Vps37a, and how this knowledge could be exploited for the development of better antagonists that could alter its trafficking and thus signaling outcomes.

STAR★METHODS

Detailed methods are provided in the online version of this paper and include the following:

- KEY RESOURCES TABLE
- RESOURCE AVAILABILITY
  - Lead contact
  - Materials availability
  - Data and code availability
- EXPERIMENTAL MODEL AND SUBJECT DETAILS
  - Human samples
  - Animals
  - Cell lines
- METHOD DETAILS
  - Vps37a overexpression constructs
  - Synthesis of Cy5-glucagon
  - Synthesis of IUB396
  - Vps37a silencing via LNPs
  - *In vivo* injections
  - Serum parameters
  - Amino acid measurements by MS/MS
  - Triglyceride and VLDL secretion assay
  - Quantitative RT–PCR analysis using SYBR Green
  - Human *VPS37A* mRNA expression studies
  - Immunoblot and quantification
  - Pulldown assay
  - Histology
  - Hepatocyte isolation and transfection
  - Stimulation experiments in primary mouse hepatocytes
  - Ligand-Induced BRET Assays
  - Immunofluorescence, EGF uptake assay and Cy5-glucagon incubations
  - Confocal microscopy and analysis
  - Vesicle 3D Reconstruction, PSC coefficients and Co-localization threshold analysis and statistics
  - β-oxidation assay with Seahorse
  - Glucose secretion assay
  - Cholesterol secretion assay
  - cAMP, glycogen and insulin measurements
- QUANTIFICATION AND STATISTICAL ANALYSIS

SUPPLEMENTAL INFORMATION

Supplemental information can be found online at https://doi.org/10.1016/j.cmet.2022.09.022.

ACKNOWLEDGMENTS

We acknowledge J. Trejo, D. Drucker, Ü. Coskun, and A. Messias for helpful discussions. We thank J. Biebl and Q. Reinold for mouse work, the pathology core facility for H&E stainings, and I. Patten for editorial support. L. Harrison created the graphical abstract in Biorender. This work was financially supported by the German Research Foundation (DFG) grant ZE1037/1-3, EFSD grant 01KU1501C, BMBF grant 16LW0116k, and Marie Sklodowska-Curie ITN, EU Horizon 2020 (EndoConnect) to A.Z.; DFG-TRR152, DFG-TRR296, DFG-SFB1123, GRK2816, DZD, and the ERC-coG Trusted 101044445 to T.D.M.; DFG-CRC/TRR333 and AMPro funding from the Helmholtz Association to S.H. N.K. is funded by Emmy-Noether DFG (KR5166/1-1). C.B. was supported by the DFG within the Munich Cluster for Systems Neurology (EXC 2145 SyNergy—ID 390857198) and the CRC 1177 (ID 259130777).

AUTHOR CONTRIBUTIONS

A.Z. designed and directed the project and R.S. designed the experiments. R.S. and K.M. performed experiments. K.M. developed the overexpression construct. Y.K. performed western blots and image analysis. A.N. and T.D.M. designed $G_{\alpha s}$ experiments, and T.D.M. provided Gcgr KO mice. J.J. and C.B. performed protein purification and pull-down experiments. B.N.,

S.W., and D.H. helped with western blots and animal experiments. A.-L.W. and O.P. designed and synthesized Cy5-glucagon. S.S. performed qPCRs. S.G., S.K., M.R., and M.B. provided patient samples and performed correlation analysis. B.Y. and B.F. synthesized IUB396. K.S. and J.G.O. measured serum amino acids. N.K., M.M., and S.H. helped in experimental design. A.Z. and R.S. wrote the manuscript.

DECLARATION OF INTERESTS

B.F. and B.Y. are employees of Novo Nordisk.

Received: January 17, 2022
Revised: August 4, 2022
Accepted: September 21, 2022
Published: October 14, 2022

REFERENCES

Abdullah, N., Beg, M., Soares, D., Dittman, J.S., and McGraw, T.E. (2016). Downregulation of a GPCR by beta-Arrestin2-mediated switch from an endosomal to a TGN recycling pathway. Cell Rep. *17*, 2966–2978.

Akinc, A., Querbes, W., De, S., Qin, J., Frank-Kamenetsky, M., Jayaprakash, K.N., Jayaraman, M., Rajeev, K.G., Cantley, W.L., Dorkin, J.R., et al. (2010). Targeted delivery of RNAi therapeutics with endogenous and exogenous ligand-based mechanisms. Mol. Ther. *18*, 1357–1364.

Altarejos, J.Y., and Montminy, M. (2011). CREB and the CRTC co-activators: sensors for hormonal and metabolic signals. Nat. Rev. Mol. Cell Biol. *12*, 141–151.

Ansarullah, Jain, C., Far, F.F., Homberg, S., Wißmiller, K., von Hahn, F.G., Raducanu, A., Schirge, S., Sterr, M., Bilekova, S., et al. (2021). Inceptor counteracts insulin signalling in β-cells to control glycaemia. Nature *590*, 326–331.

Apostolopoulou, M., Gordillo, R., Koliaki, C., Gancheva, S., Jelenik, T., De Filippo, E., Herder, C., Markgraf, D., Jankowiak, F., Esposito, I., et al. (2018). Specific hepatic sphingolipids relate to insulin resistance, oxidative stress, and inflammation in nonalcoholic steatohepatitis. Diabetes Care *41*, 1235–1243.

Authier, F., and Desbuquois, B. (2008). Glucagon receptors. Cell. Mol. Life Sci. *65*, 1880–1899.

Bache, K.G., Slagsvold, T., Cabezas, A., Rosendal, K.R., Raiborg, C., and Stenmark, H. (2004). The growth-regulatory protein HCRP1/hVps37A is a subunit of mammalian ESCRT-I and mediates receptor down-regulation. Mol. Biol. Cell *15*, 4337–4346.

Berg, K.A., and Clarke, W.P. (2018). Making sense of pharmacology: inverse agonism and functional selectivity. Int. J. Neuropsychopharmacol. *21*, 962–977.

Blüher, M., Unger, R., Rassoul, F., Richter, V., and Paschke, R. (2002). Relation between glycaemic control, hyperinsulinaemia and plasma concentrations of soluble adhesion molecules in patients with impaired glucose tolerance or Type II diabetes. Diabetologia *45*, 210–216.

Bogorad, R.L., Yin, H., Zeigerer, A., Nonaka, H., Ruda, V.M., Zerial, M., Anderson, D.G., and Koteliansky, V. (2014). Nanoparticle-formulated siRNA targeting integrins inhibits hepatocellular carcinoma progression in mice. Nat. Commun. *5*, 3869.

Bomholt, A.B., Johansen, C.D., Kjeldsen, S.A.S., Galsgaard, K.D., Christensen, J.B., Winther-Sørensen, M., Serizawa, R., Hornum, M., Porrini, E., Pedersen, J., et al. (2021). Evaluation of commercially available glucagon receptor antibodies and glucagon receptor expression. Preprint at bioRxiv. https://doi.org/10.1101/2021.12.21.473442.

Bühler, L., Maida, A., Vogl, E.S., Georgiadi, A., Takacs, A., Kluth, O., Schürmann, A., Feuchtinger, A., von Toerne, C., Tsokanos, F.F., et al. (2021). Lipocalin 13 enhances insulin secretion but is dispensable for systemic metabolic control. Life Sci. Alliance *4*, e202000898.

Bush, A., Vasen, G., Constantinou, A., Dunayevich, P., Patop, I.L., Blaustein, M., and Colman-Lerner, A. (2016). Yeast GPCR signaling reflects the fraction of occupied receptors, not the number. Mol. Syst. Biol. *12*, 898.

Cajulao, J.M.B., Hernandez, E., von Zastrow, M.E., and Sanchez, E.L. (2022). Glucagon receptor-mediated regulation of gluconeogenic gene transcription is endocytosis-dependent in primary hepatocytes. Mol. Biol. Cell *33*, ar90.

Challa, T.D., Wueest, S., Lucchini, F.C., Dedual, M., Modica, S., Borsigova, M., Wolfrum, C., Blüher, M., and Konrad, D. (2019). Liver ASK1 protects from non-alcoholic fatty liver disease and fibrosis. EMBO Mol. Med. *11*, e10124.

Clark, L.J., Krieger, J., White, A.D., Bondarenko, V., Lei, S., Fang, F., Lee, J.Y., Doruker, P., Böttke, T., Jean-Alphonse, F., et al. (2020). Allosteric interactions in the parathyroid hormone GPCR-arrestin complex formation. Nat. Chem. Biol. *16*, 1096–1104.

Eichel, K., and von Zastrow, M. (2018). Subcellular organization of GPCR signaling. Trends Pharmacol. Sci. *39*, 200–208.

Feng, G.H., Lih, C.J., and Cohen, S.N. (2000). TSG101 protein steady-state level is regulated posttranslationally by an evolutionarily conserved COOH-terminal sequence. Cancer Res. *60*, 1736–1741.

Ferrandon, S., Feinstein, T.N., Castro, M., Wang, B., Bouley, R., Potts, J.T., Gardella, T.J., and Vilardaga, J.P. (2009). Sustained cyclic AMP production by parathyroid hormone receptor endocytosis. Nat. Chem. Biol. *5*, 734–742.

Feuchtinger, A., Stiehler, T., Jütting, U., Marjanovic, G., Luber, B., Langer, R., and Walch, A. (2015). Image analysis of immunohistochemistry is superior to visual scoring as shown for patient outcome of esophageal adenocarcinoma. Histochem. Cell Biol. *143*, 1–9.

French, A.P., Mills, S., Swarup, R., Bennett, M.J., and Pridmore, T.P. (2008). Colocalization of fluorescent markers in confocal microscope images of plant cells. Nat. Protoc. *3*, 619–628.

Galsgaard, K.D., Pedersen, J., Knop, F.K., Holst, J.J., and Wewer Albrechtsen, N.J. (2019). Glucagon receptor signaling and lipid metabolism. Front. Physiol. *10*, 413.

Gilliland, C.T., Salanga, C.L., Kawamura, T., Trejo, J., and Handel, T.M. (2013). The chemokine receptor CCR1 is constitutively active, which leads to G protein-independent, beta-arrestin-mediated internalization. J. Biol. Chem. *288*, 32194–32210.

Godbole, A., Lyga, S., Lohse, M.J., and Calebiro, D. (2017). Internalized TSH receptors en route to the TGN induce local Gs-protein signaling and gene transcription. Nat. Commun. *8*, 443.

Godoy, P., Hewitt, N.J., Albrecht, U., Andersen, M.E., Ansari, N., Bhattacharya, S., Bode, J.G., Bolleyn, J., Borner, C., Böttger, J., et al. (2013). Recent advances in 2D and 3D in vitro systems using primary hepatocytes, alternative hepatocyte sources and non-parenchymal liver cells and their use in investigating mechanisms of hepatotoxicity, cell signaling and ADME. Arch. Toxicol. *87*, 1315–1530.

Habegger, K.M., Heppner, K.M., Geary, N., Bartness, T.J., DiMarchi, R., and Tschöp, M.H. (2010). The metabolic actions of glucagon revisited. Nat. Rev. Endocrinol. *6*, 689–697.

Harayama, T., and Riezman, H. (2018). Understanding the diversity of membrane lipid composition. Nat. Rev. Mol. Cell Biol. *19*, 281–296.

Herzig, S., Long, F., Jhala, U.S., Hedrick, S., Quinn, R., Bauer, A., Rudolph, D., Schutz, G., Yoon, C., Puigserver, P., et al. (2001). CREB regulates hepatic gluconeogenesis through the coactivator PGC-1. Nature *413*, 179–183.

Hjorth, S.A., Orskov, C., and Schwartz, T.W. (1998). Constitutive activity of glucagon receptor mutants. Mol. Endocrinol. *12*, 78–86.

Hogan, M.F., Ravnskjaer, K., Matsumura, S., Huising, M.O., Hull, R.L., Kahn, S.E., and Montminy, M. (2015). Hepatic insulin resistance following chronic activation of the CREB coactivator CRTC2. J. Biol. Chem. *290*, 25997–26006.

Hurley, J.H. (2010). The ESCRT complexes. Crit. Rev. Biochem. Mol. Biol. *45*, 463–487.

Irannejad, R., Tomshine, J.C., Tomshine, J.R., Chevalier, M., Mahoney, J.P., Steyaert, J., Rasmussen, S.G., Sunahara, R.K., El-Samad, H., Huang, B., et al. (2013). Conformational biosensors reveal GPCR signalling from endosomes. Nature *495*, 534–538.

Janah, L., Kjeldsen, S., Galsgaard, K.D., Winther-Sørensen, M., Stojanovska, E., Pedersen, J., Knop, F.K., Holst, J.J., and Wewer Albrechtsen, N.J. (2019). Glucagon receptor signaling and glucagon resistance. Int. J. Mol. Sci. *20*, 3314.

Kimball, S.R., Siegfried, B.A., and Jefferson, L.S. (2004). Glucagon represses signaling through the mammalian target of rapamycin in rat liver by activating AMP-activated protein kinase. J. Biol. Chem. *279*, 54103–54109.

Kirshner, H., Aguet, F., Sage, D., and Unser, M. (2013). 3-D PSF fitting for fluorescence microscopy: implementation and localization application. J. Microsc. *249*, 13–25.

Klöting, N., Fasshauer, M., Dietrich, A., Kovacs, P., Schön, M.R., Kern, M., Stumvoll, M., and Blüher, M. (2010). Insulin-sensitive obesity. Am. J. Physiol. Endocrinol. Metab. *299*, E506–E515.

Koliaki, C., Szendroedi, J., Kaul, K., Jelenik, T., Nowotny, P., Jankowiak, F., Herder, C., Carstensen, M., Krausch, M., Knoefel, W.T., et al. (2015). Adaptation of hepatic mitochondrial function in humans with non-alcoholic fatty liver is lost in steatohepatitis. Cell Metab. *21*, 739–746.

Kolmus, K., Erdenebat, P., Szymańska, E., Stewig, B., Goryca, K., Derezińska-Wołek, E., Szumera-Ciećkiewicz, A., Brewińska-Olchowik, M., Piwocka, K., Prochorec-Sobieszek, M., et al. (2021). Concurrent depletion of Vps37 proteins evokes ESCRT-I destabilization and profound cellular stress responses. J. Cell Sci. *134*, jcs250951.

Krahmer, N., Najafi, B., Schueder, F., Quagliarini, F., Steger, M., Seitz, S., Kasper, R., Salinas, F., Cox, J., Uhlenhaut, N.H., et al. (2018). Organellar proteomics and phospho-proteomics reveal subcellular reorganization in diet-induced hepatic steatosis. Dev. Cell *47*, 205–221.e7.

Krilov, L., Nguyen, A., Miyazaki, T., Unson, C.G., and Bouscarel, B. (2008). Glucagon receptor recycling: role of carboxyl terminus, beta-arrestins, and cytoskeleton. Am. J. Physiol. Cell Physiol. *295*, C1230–C1237.

Lan, T.H., Kuravi, S., and Lambert, N.A. (2011). Internalization dissociates beta2-adrenergic receptors. PLoS One *6*, e17361.

Longuet, C., Sinclair, E.M., Maida, A., Baggio, L.L., Maziarz, M., Charron, M.J., and Drucker, D.J. (2008). The glucagon receptor is required for the adaptive metabolic response to fasting. Cell Metab. *8*, 359–371.

Longuet, C., Robledo, A.M., Dean, E.D., Dai, C., Ali, S., McGuinness, I., de Chavez, V., Vuguin, P.M., Charron, M.J., Powers, A.C., et al. (2013). Liver-specific disruption of the murine glucagon receptor produces alpha-cell hyperplasia: evidence for a circulating alpha-cell growth factor. Diabetes *62*, 1196–1205.

Mantovani, A., Byrne, C.D., Bonora, E., and Targher, G. (2018). Nonalcoholic fatty liver disease and risk of incident type 2 diabetes: a meta-analysis. Diabetes Care *41*, 372–382.

Marchese, A., and Trejo, J. (2013). Ubiquitin-dependent regulation of G protein-coupled receptor trafficking and signaling. Cell. Signal. *25*, 707–716.

Mattedi, G., Acosta-Gutiérrez, S., Clark, T., and Gervasio, F.L. (2020). A combined activation mechanism for the glucagon receptor. Proc. Natl. Acad. Sci. USA *117*, 15414–15422.

Maziarz, M., Park, J.C., Leyme, A., Marivin, A., Garcia-Lopez, A., Patel, P.P., and Garcia-Marcos, M. (2020). Revealing the activity of trimeric G-proteins in live cells with a versatile biosensor design. Cell *182*, 770–785.e16.

McDonald, B., and Martin-Serrano, J. (2008). Regulation of Tsg101 expression by the steadiness box: a role of Tsg101-associated ligase. Mol. Biol. Cell *19*, 754–763.

McGlone, E.R., Manchanda, Y., Jones, B., Pickford, P., Inoue, A., Carling, D., Bloom, S.R., Tan, T., and Tomas, A. (2021). Receptor activity-modifying protein 2 (RAMP2) alters glucagon receptor trafficking in hepatocytes with functional effects on receptor signalling. Mol. Metab. *53*, 101296.

Miaczynska, M. (2013). Effects of membrane trafficking on signaling by receptor tyrosine kinases. Cold Spring Harb. Perspect. Biol. *5*, a009035.

Müller, T.D., Finan, B., Clemmensen, C., DiMarchi, R.D., and Tschöp, M.H. (2017). The new biology and pharmacology of glucagon. Physiol. Rev. *97*, 721–766.

O'Banion, C.P., Vickerman, B.M., Haar, L., and Lawrence, D.S. (2019). Compartmentalized cAMP generation by engineered photoactivated adenylyl cyclases. Cell Chem. Biol. *26*, 1393–1406.e7.

Okumura, M., Katsuyama, A.M., Shibata, H., and Maki, M. (2013). VPS37 isoforms differentially modulate the ternary complex formation of ALIX, ALG-2, and ESCRT-I. Biosci. Biotechnol. Biochem. *77*, 1715–1721.

Perry, R.J., Zhang, D., Guerra, M.T., Brill, A.L., Goedeke, L., Nasiri, A.R., Rabin-Court, A., Wang, Y., Peng, L., Dufour, S., et al. (2020). Glucagon stimulates gluconeogenesis by INSP3R1-mediated hepatic lipolysis. Nature *579*, 279–283.

Petersen, M.C., Vatner, D.F., and Shulman, G.I. (2017). Regulation of hepatic glucose metabolism in health and disease. Nat. Rev. Endocrinol. *13*, 572–587.

Rizza, R.A. (2010). Pathogenesis of fasting and postprandial hyperglycemia in type 2 diabetes: implications for therapy. Diabetes *59*, 2697–2707.

Sage, D., Donati, L., Soulez, F., Fortun, D., Schmit, G., Seitz, A., Guiet, R., Vonesch, C., and Unser, M. (2017). DeconvolutionLab2: an open-source software for deconvolution microscopy. Methods *115*, 28–41.

Sakai, M., Matsumoto, M., Tujimura, T., Yongheng, C., Noguchi, T., Inagaki, K., Inoue, H., Hosooka, T., Takazawa, K., Kido, Y., et al. (2012). CITED2 links hormonal signaling to PGC-1α acetylation in the regulation of gluconeogenesis. Nat. Med. *18*, 612–617.

Sammons, M.F., and Lee, E.C. (2015). Recent progress in the development of small-molecule glucagon receptor antagonists. Bioorg. Med. Chem. Lett. *25*, 4057–4064.

Samuel, V.T., and Shulman, G.I. (2016). The pathogenesis of insulin resistance: integrating signaling pathways and substrate flux. J. Clin. Invest. *126*, 12–22.

Scarselli, M., and Donaldson, J.G. (2009). Constitutive internalization of G protein-coupled receptors and G proteins via clathrin-independent endocytosis. J. Biol. Chem. *284*, 3577–3585.

Scheen, A.J., Paquot, N., and Lefèbvre, P.J. (2017). Investigational glucagon receptor antagonists in Phase I and II clinical trials for diabetes. Expert Opin. Investig. Drugs *26*, 1373–1389.

Schmidt, O., and Teis, D. (2012). The ESCRT machinery. Curr. Biol. *22*, R116–R120.

Seifert, R., and Wenzel-Seifert, K. (2002). Constitutive activity of G-protein-coupled receptors: cause of disease and common property of wild-type receptors. Naunyn Schmiedebergs Arch. Pharmacol. *366*, 381–416.

Seitz, S., Kwon, Y., Hartleben, G., Jülg, J., Sekar, R., Krahmer, N., Najafi, B., Loft, A., Gancheva, S., Stemmer, K., et al. (2019). Hepatic Rab24 controls blood glucose homeostasis via improving mitochondrial plasticity. Nat. Metab. *1*, 1009–1026.

Stuffers, S., Brech, A., and Stenmark, H. (2009). ESCRT proteins in physiology and disease. Exp. Cell Res. *315*, 1619–1626.

Sutkeviciute, I., and Vilardaga, J.P. (2020). Structural insights into emergent signaling modes of G protein-coupled receptors. J. Biol. Chem. *295*, 11626–11642.

Szymanska, E., Budick-Harmelin, N., and Miaczynska, M. (2018). Endosomal "sort" of signaling control: the role of ESCRT machinery in regulation of receptor-mediated signaling pathways. Semin. Cell Dev. Biol. *74*, 11–20.

Thomsen, A.R.B., Plouffe, B., Cahill, T.J., 3rd, Shukla, A.K., Tarrasch, J.T., Dosey, A.M., Kahsai, A.W., Strachan, R.T., Pani, B., Mahoney, J.P., et al. (2016). GPCR-G protein-beta-arrestin super-complex mediates sustained G protein signaling. Cell *166*, 907–919.

Tsvetanova, N.G., and von Zastrow, M. (2014). Spatial encoding of cyclic AMP signaling specificity by GPCR endocytosis. Nat. Chem. Biol. *10*, 1061–1065.

Vilardaga, J.P., Jean-Alphonse, F.G., and Gardella, T.J. (2014). Endosomal generation of cAMP in GPCR signaling. Nat. Chem. Biol. *10*, 700–706.

Wan, Q., Okashah, N., Inoue, A., NehmeNehmé, R., Carpenter, B., Tate, C.G., and Lambert, N.A. (2018). Mini G protein probes for active G protein-coupled receptors (GPCRs) in live cells. J. Biol. Chem. *293*, 7466–7473.

Weis, W.I., and Kobilka, B.K. (2018). The molecular basis of G protein-coupled receptor activation. Annu. Rev. Biochem. *87*, 897–919.

Yang, B., Gelfanov, V.M., Perez-Tilve, D., DuBois, B., Rohlfs, R., Levy, J., Douros, J.D., Finan, B., Mayer, J.P., and DiMarchi, R.D. (2021). Optimization of truncated glucagon peptides to achieve selective, high potency, full antagonists. J. Med. Chem. *64*, 4697–4708.

Yen, H.Y., Hoi, K.K., Liko, I., Hedger, G., Horrell, M.R., Song, W., Wu, D., Heine, P., Warne, T., Lee, Y., et al. (2018). PtdIns(4,5)P2 stabilizes active states of GPCRs and enhances selectivity of G-protein coupling. Nature *559*, 423–427.

Zeigerer, A., Gilleron, J., Bogorad, R.L., Marsico, G., Nonaka, H., Seifert, S., Epstein-Barash, H., Kuchimanchi, S., Peng, C.G., Ruda, V.M., et al. (2012). Rab5 is necessary for the biogenesis of the endolysosomal system *in vivo*. Nature *485*, 465–470.

Zeigerer, A., Bogorad, R.L., Sharma, K., Gilleron, J., Seifert, S., Sales, S., Berndt, N., Bulik, S., Marsico, G., D'Souza, R.C.J., et al. (2015). Regulation of liver metabolism by the endosomal GTPase Rab5. Cell Rep. *11*, 884–892.

Zeigerer, A., Wuttke, A., Marsico, G., Seifert, S., Kalaidzidis, Y., and Zerial, M. (2017). Functional properties of hepatocytes in vitro are correlated with cell polarity maintenance. Exp. Cell Res. *350*, 242–252.

Zeigerer, A., Sekar, R., Kleinert, M., Nason, S., Habegger, K.M., and Müller, T.D. (2021). Glucagon's metabolic action in health and disease. Compr. Physiol. *11*, 1759–1783.

Zellmer, S., Schmidt-Heck, W., Godoy, P., Weng, H., Meyer, C., Lehmann, T., Sparna, T., Schormann, W., Hammad, S., Kreutz, C., et al. (2010). Transcription factors ETF, E2F, and SP-1 are involved in cytokine-independent proliferation of murine hepatocytes. Hepatology *52*, 2127–2136.

Zhao, G.N., Zhang, P., Gong, J., Zhang, X.J., Wang, P.X., Yin, M., Jiang, Z., Shen, L.J., Ji, Y.X., Tong, J., et al. (2017). Tmbim1 is a multivesicular body regulator that protects against non-alcoholic fatty liver disease in mice and monkeys by targeting the lysosomal degradation of Tlr4. Nat. Med. *23*, 742–752.

Zhu, L., Rossi, M., Cui, Y., Lee, R.J., Sakamoto, W., Perry, N.A., Urs, N.M., Caron, M.G., Gurevich, V.V., Godlewski, G., et al. (2017). Hepatic beta-arrestin 2 is essential for maintaining euglycemia. J. Clin. Invest. *127*, 2941–2945.

STAR★METHODS

KEY RESOURCES TABLE

REAGENT or RESOURCE	SOURCE	IDENTIFIER
Antibodies		
Vps37a (WB)	Atlas Antibodies	Cat# HPA024705; RRID: AB_10601776
Vps37a (IF)	Proteintech	Cat# 11870-1-AP; RRID: AB_2215230
p-AMPKα (Thr 172)	Cell Signaling	Cat# 2535; RRID: AB_331250
AMPKα (23A3)	Cell Signaling	Cat# 2603; RRID: AB_490795
ACCα	Abcam	Cat# ab72046; RRID: AB_2219412
p-ACC (Ser79)	Cell Signaling	Cat# 3663; RRID: AB_2172866
Vinculin	Abcam	Cat# ab129002; RRID: AB_11144129
VCP	Abcam	Cat# ab11433; RRID: AB_298039
p-Creb (Se133)	Cell Signaling	Cat# 9198; RRID: AB_2561044
Creb (48H2)	Cell Signaling	Cat# 9197; RRID: AB_331277
p-Foxo1 (Ser256)	Cell Signaling	Cat# 9461; RRID: AB_329831
Foxo1	Cell Signaling	Cat# 2880; RRID: AB_2106495
Pkc epsilon	BD biosciences	Cat# 610086; RRID: AB_397493
CAMKII-a	Cell Signaling	Cat# 50049; RRID: AB_2721906
p-CAMKII-a (Thr286)	Novus biologicals	Cat# NB300184; RRID: AB_2068102
Akt	Cell Signaling	Cat# 9272; RRID: AB_329827
p-Akt (Ser473)	Cell Signaling	Cat# 4060; RRID: AB_2315049
Fas	Cell Signaling	Cat# 3180; RRID: AB_2100796
Vps37b	Atlas Antibodies	Cat# HPA038217; RRID: AB_10672740
Vps37c	Abcam	Cat# ab151753; RRID: AB_2923176
Vps28	Santa Cruz	Cat# sc166514; RRID: AB_2214883
Tsg101	Abcam	Cat# ab30871; RRID: AB_2208084
Glucagon receptor	Abcam	Cat# ab75240; RRID: AB_1523687
Beta 2 adrenergic receptor	Abcam	Cat# ab182136; RRID: AB_2747383
Insulin receptor beta subunit (IRß)	SantaCruz	Cat# sc-711; RRID: AB_631835
EEA1	Thermo Fisher	Cat# 17228; RRID: AB_11004515
Rab11	BD Biosciences	Cat# 610657; RRID: AB_397984
Lamp1 (mouse)	BD Biosciences	Cat# 553792; RRID: AB_2134499
Lamp1 (human)	BD Biosciences	Cat# 553798; RRID: AB_396132
BIODIPY 493/503	Thermo Fisher Scientific	Cat# D3922
Alexa 555 goat anti-rabbit	Thermo Fisher Scientific	Cat# A-21429; RRID: AB_2535850
Alexa 647 goat anti-rabbit	Thermo Fisher Scientific	Cat# A-21244; RRID: AB_2535812
Alexa 555 goat anti-rat	Thermo Fisher Scientific	Cat# A-21434; RRID: AB_2535855
Alexa 647 goat anti-rat	Thermo Fisher Scientific	Cat# A-21247; RRID: AB_141778
Alexa 488 phalloidin	Thermo Fisher Scientific	Cat# A12379
EGF-555	Thermo Fisher Scientific	Cat# E35350
Goat anti-rabbit HRP	Sigma Aldrich	Cat# A6154; RRID: AB_258284
Rabbit anti-mouse HRP	Thermo Fisher Scientific	Cat# 61-6520; RRID: AB_2533933
Bacterial and virus strains		
AAV8-LP1-mVps37a	This Study	N/A
AAV8-LP1-GFPmut	Bühler et al., 2021	N/A
Biological samples		
Cryopreserved primary human hepatocytes	Lonza	N/A

(*Continued on next page*)

Continued

REAGENT or RESOURCE	SOURCE	IDENTIFIER
Chemicals, peptides, and recombinant proteins		
Cy-5-Glucagon	This Study	N/A
Glucagon	Millipore	Cat# 05-23-2700
IUB396	Yang et al., 2021	N/A
Huminsulin Normal 100	Lilly	HI0210
Sodium pyruvate	Sigma-Aldrich	Cat# P2580
cOmplete EDTA-free Protease Inhibitor Cocktail	Roche	Cat# 11836170001
Phosphostop- phosphatase inhibitor tablets	Roche	Cat# 4906845001
TRIzol	Life Technologies	Cat# 15596018
Tyloxapol	Sigma-Aldrich	Cat# 25301-02-4
DAPI	Life Technologies	Cat# D3571
MOWIOL 4-88 reagent	Merck Millipore	Cat# 475904
Amersham ECL Prime	Cytiva	Cat# RPN2232
William's Medium E	PAN-Biotech	Cat# P04-29500
Rat tail Collagen 1	Sigma-Aldrich	Cat# 11179179001
DMEM	Life Technologies	Cat# 11995073
Sera Plus (Special Processed FBS)	PAN-Biotech	Cat# P30-3702
Collagenase	Sigma-Aldrich	Cat# C5138-1G
FBS	Life Technologies	Cat# 10500064
dexamethasone	Sigma-Aldrich	Cat# D4902
penicillin-streptomycin	Sigma-Aldrich	Cat# P4333
interferin	Polyplus	Cat# 40950
Lipofectamine 2000	Invitrogen	Cat# 11668019
Forskolin	Sigma-Aldrich	Cat# F3917
Isoproterenol	Sigma-Aldrich	Cat# I2760
Critical commercial assays		
Insulin Elisa kit	Alpco	Cat# 80-INSMS-E01
Triglyceride assay kit	Abcam	Cat# ab65336
Glycogen kit	Sigma-Aldrich	Cat# MAK016
Glucagon Elisa kit	Mercodia	Cat# 10-1271-01
Amplex Red Glucose Assay Kit	Thermo Fisher Scientific	Cat# A22189
Amplex Red Cholesterol Assay Kit	Thermo Fisher Scientific	Cat# A12216
cAMP direct immunoassay kit	Abcam	Cat# ab65355
Bio-Rad Protein Assay Kit II	Bio-Rad	Cat# 5000002
QuantiTect Reverse Transcription Kit	Qiagen	Cat# 205311
Experimental models: Cell lines		
HEK293T	ATCC	Cat# CRL-3216
Experimental models: Organisms/strains		
C57BL/6N	Charles River	Strain code: 027
C57BL/6N	Janvier	SC-C57N-M
C57Bl/6-*Gcgr*$^{Hep-/-}$	Longuet et al., 2013	From Prof. Timo D. Müller
BKS(D)-Leprdb/JOrlRj (homozygous)	Janvier	SM-DB-M
BKS(D)-Leprdb/JOrlRj (heterozygous)	Janvier	SM-DB-M
Oligonucleotides		
Primer sequence for qRT-PCR	N/A	Table S5
Taqman Probe VPS37A	Thermo Fisher Scientific	Cat# 4331182; Hs01001503_g1
Taqman Probe 18S rRNA	Thermo Fisher Scientific	Cat# 4333760; Hs99999901_s1

(*Continued on next page*)

Continued

REAGENT or RESOURCE	SOURCE	IDENTIFIER
siRNA targeting Vps37a in LNP: Vps37a: sense 5′-cguAcAGA uuAGAauGAcAdTsdT-3' antisense 5′-UGUcAUUCuAAUCUG uACGdTsdT-3'	This paper (Axolabs)	N/A
siRNA luciferase: sense 5′-cuuAcGcuGAGuAcuucGAdTsdT-3′, antisense 5′-UCGAAGuACUcAGCGuAAGdTsdT-3′.	This paper (Axolabs)	N/A
Tsg101 siRNA	Dharmacon	Cat# L-049922-01
Vps37b siRNA	Dharmacon	Cat# L-057449-01
Vps37c siRNA	Dharmacon	Cat# L-063041-01
Vps28 siRNA	Dharmacon	Cat# L-045159-01
β-arrestin-2 siRNA	Dharmacon	Cat# L-041022-01
Recombinant DNA		
Plasmid: pdsAAV2-LP1-mVps37a	This Study	N/A
Plasmid: pdsAAV2-LP1-GFPmut	Bühler et al., 2021	N/A
Untagged GcgR	BioCat GmbH	Cat# EX-A0475-M02-10-GC
GcgR-eGFP	BioCat GmbH	Cat# EX-A0475-M98-10-GC
NES-Nluc-MiniGF061$_s$	Lan et al., 2011; Wan et al., 2018	Kind gift from Professor Kevin Pfleger (Harry Perkins Institute of Medical Research, Nedlands, WA, Australia)
Venus-Rab5a (early endosomes)	Lan et al., 2011; Wan et al., 2018	Kind gift from Professor Kevin Pfleger (Harry Perkins Institute of Medical Research, Nedlands, WA, Australia)
Gβγ-BERKY3	Maziarz et al., 2020	Kind gift from Maziarz et al. (2020)
Software and algorithms		
ImageJ (Fiji)	ImageJ, v.2.0.0-rc-69/1.52p	https://imagej.net/software/fiji/
Graphpad Prism 8	GraphPad Software	https://www.graphpad.com
KaleidaGraph v5	Synergy Software	https://www.synergy.com/
Other		
Power SYBR Green PCR Master Mix	Thermo Fisher Scientific	Cat# 4367659
Insulin Syringe Volume: 3/10 cc; 29G x 0.5 in. Ultra-Fine permanently attached needle	BD (Fisher)	Cat# 309301
SuperSignal West Pico PLUS Chemiluminescent Substrate	Thermo Fisher Scientific	Cat# 34580
SuperSignal West Femto Maximum Sensitivity Substrate	Thermo Fisher Scientific	Cat# 34096
NanoLuciferase substrate NanoGlo	Promega	Cat #: N1110
High Fat Diet 60%	Research Diets	D12492i
Novex WedgeWell 8–16% or 4-20% Tris-Glycine Mini Gels	Thermo Fisher Scientific	Cat# XP08162BOX

RESOURCE AVAILABILITY

Lead contact

Further information and requests for resources and reagents may be sent to and will be answered by the lead contact, Anja Zeigerer (anja.zeigerer@helmholtz-muenchen.de).

Materials availability

Plasmids generated in this study will be made available on request to the lead contact.

Data and code availability

- All relevant data used for this publication are included in Data S1.
- This paper does not report original code.
- Any additional information required to reanalyze the data reported in this paper is available from the lead contact upon request.

EXPERIMENTAL MODEL AND SUBJECT DETAILS

Human samples

The first cohort comprised up to thirty-six individuals with obesity (OBE; n=9 males and n=27 females; average age of 42.5 ± 1.67 yrs.) undergoing bariatric surgery and 9 lean healthy individuals (CON; n=3 males and n=6 females; average age 42.6 ± 3.43 yrs.) undergoing elective surgery such as cholecystectomy or herniotomy (registered clinical trial NCT01477957), part of which were previously reported (Apostolopoulou et al., 2018; Koliaki et al., 2015). OBE were further classified into obese with steatosis (NAFL+), without steatosis (NAFL-), and NASH based on liver histology as described in Apostolopoulou et al. (2018) and Koliaki et al. (2015). The patients gave written informed consent before inclusion in the study, which was approved by the Heinrich-Heine-University Düsseldorf Institutional Review Board. All participants maintained stable body weight for at least 2 weeks before surgery and were studied using hyperinsulinemic euglycemic clamps for measurement of peripheral and hepatic insulin sensitivity and blood sampling for routine lab parameters (Koliaki et al., 2015). Participants were asked to refrain from physical activity for 3 days prior to the clamp test. Volunteers with severe renal, heart or lung disease, acute or chronic inflammatory condition or any history or signs of liver disease other than NAFLD were excluded from participation. Liver samples for measurement of liver fat content from histology, hepatic mitochondrial function and oxidative stress were obtained during surgery as described before (Koliaki et al., 2015). No statistical method has been used to predetermine sample size.

The second cohort comprises of 66 extensively characterized Caucasian men (n=37) and women (n=29), average age 64.7 ± 1.58 yrs., with a wide range of body mass index (BMI: 22.7-45.6 kg/m^2), who underwent open abdominal surgery for Roux en Y bypass, sleeve gastrectomy, elective cholecystectomy or explorative laparotomy. BMI was calculated as weight divided by squared height. Hip circumference was measured over the buttocks; waist circumference was measured at the midpoint between the lower ribs and iliac crest. Percentage body fat was measured by dual X-ray absorptiometry or bioimpedance analyses. In addition, abdominal visceral and SC fat areas were calculated using CT or MRI scans at the level of L4–L5. With oral glucose tolerance tests, we identified individuals with normal glucose tolerance (n=40). Methods of the phenotypic characterization have been described previously (Klöting et al., 2010). Insulin sensitivity was assessed with the euglycemic-hyperinsulinemic clamp method. After an overnight fast and resting for 30min in a supine position, intravenous catheters were inserted into antecubital veins in both arms of the participants. One line was used for the infusion of insulin and glucose, the other was used for frequent sampling of arterialized (heating pads) blood. After a priming dose of 1.2nmol/m^2 insulin, infusion with insulin (Actrapid 100U/ml, Novo Nordisk Bagsvaerd, Denmark) was started with a constant infusion rate of 0.28nmol/m^2 body surface per minute and continued for at least 120min. After 3min, the variable 20% glucose infusion rate was added and adjusted during the clamp to maintain a blood glucose level of 5.5 (± 5%) mmol/l. Bedside blood glucose measurements were carried out every 5min. Glucose infusion rate (GIR) was calculated from the last 45 min of the clamp, in which GIR could be kept constant to achieve the target plasma glucose concentration of 5.5 mmol/l. Therefore, the duration of the clamp varied between individuals (range 120–200 min). In premenopausal women, clamp studies were performed during the luteal phase of the menstrual cycle (Blüher et al., 2002; Challa et al., 2019).

All baseline blood samples were collected between 8 and 10 am after an overnight fast. Samples were immediately centrifuged and stored at -80°C until further analyses were performed. Plasma glucose levels were measured using the hexokinase method. Insulin was measured using chemiluminescence assay. High-density lipoprotein (HDL) cholesterol and low-density lipoprotein (LDL) cholesterol were measured using enzymatic assays (COBAS, Roche, Mannheim, Germany). CRP was quantified using an Image Automatic Immunoassay System (Beckman Coulter). Circulating levels of high-sensitivity interleukin 6 (hsIL 6), leptin (R&D Systems, Minneapolis, MN), and total adiponectin (ALPCO, Salem, NH) were determined in all blood samples with enzyme-linked immunosorbent assays (ELISAs) according to the manufacturers' instructions. The index for homeostatic model assessment of insulin resistance (HOMA1-IR) was calculated from fasting plasma insulin and glucose measurements. All study protocols have been approved by the Ethics committee of the University of Leipzig (363-10-13122010 and 017-12-230112). All participants gave written informed consent before taking part in the study. No statistical method has been used to predetermine sample size.

Animals

All animal studies were conducted in accordance with German animal welfare legislation. Male C57BL/6N mice were obtained from the Janvier Laboratories or Charles River Laboratories and maintained in a climate-controlled environment with specific pathogen-free conditions under 12-h dark–light cycles in the animal facility of the Helmholtz Center, Munich, Germany. Protocols were approved by the institutional animal welfare officer and the necessary licenses were obtained from the state ethics committee and government of Upper Bavaria (nos. 55.2-1-55-2532-49-2017 and 55.2-1-54-2532.0-40-15). Mice were fed ad libitum with regular rodent chow. Mice for the HFD studies received a HFD or regular chow from Research Diets for 13 or 16 weeks, starting at the age of 7 weeks, according to the following diet composition: HFD: 16% protein, 25% carbohydrate, 60% fat in kcal. All experiments were carried out using male mice with littermates as controls. Sample size was not predetermined. Instead group sizes were selected based on contemporary work published. All mice were randomized for weight and blood glucose before the start of the experiments.

Gcgr^{Flox} chimeric mice carrying one loxP site between exons 5 and 6 and two loxP sites in a neomycin cassette inserted Gcgr between exons 12 and 13 of the Gcgr gene were generated in the C57Bl/6 background, and the neomycin cassette was removed using the FLPe-FRT system. *Gcgr*$^{Hep-/-}$ mice were generated by breeding *Gcgr*^{Flox} mice and Albumin-*Cre* mice, as described previously (Longuet et al., 2013).

Cell lines

HEK293T cells (ATCC) were cultured in Dulbecco's Modified Eagle Medium supplemented with 10% heat-inactivated fetal bovine serum, 100 IU/mL of penicillin, and 100 μg/mL of streptomycin solution.

METHOD DETAILS

Vps37a overexpression constructs

The Vps37a overexpression construct was generated by digesting a commercially synthesized pUC57 plasmid containing the coding sequence of murine Vps37a (NM_033560.3) (Genscript, USA) with NotI and KpnI and ligating into a pdsAAV2-LP1 backbone. As control, we used a translation deficient version of GFP, as previously published (Bühler et al., 2021). AAV packaging into AAV8 was conducted by Vigene Biosciences, USA.

Synthesis of Cy5-glucagon

Glucagon-30-Pra (01, GCG-Pra) was synthesized by standard *N*-(9-fluorenyl)methoxycarbonyl (Fmoc) chemistry. Subsequently, peptide 01 was reacted with Cyanin-5-azide in a copper-mediated click reaction to yield the Cy5-glucacon probe, which was purified by HPLC. Synthetic details are described in Methods S1.

Synthesis of IUB396

Peptide sequence TSDYSKYLDSRRAQDFVQWLMDT amide was assembled by automated Fmoc/tBu solid-phase chemistry starting with H-Rink Amide ChemMatrix (PCAS BioMatrix, Saint-Jean-sur-Richelieu, Quebec, Canada J3B 8J8) on a Symphony Peptide Synthesizer (Peptide Technology, Tucson, AZ). All Fmoc-amino acids were coupled with 6-Cl-HOBt/DIC activation in DMF. The Fmoc were removed by 20% piperidine in DMF. The N-terminal L-3-Phenyllactic acid or (S)-3- Phenyllactic acid (Sigma-Aldrich, St. Louis, MO) was coupled manually by 3-fold excess DEPBT (Diethyl 3,4-dihydro-4-oxo-1,2,3-benzotriazin-3-yl phosphate) reagent with DIEA in DMF. Peptide was cleaved from the resin with 10ml TFA cleavage cocktail containing 8.5ml TFA, 0.5ml water, 0.5ml Tis (triisopropylsilane), 0.25g phenol and 0.25ml 2-mercaptoethanol for 2h. Peptide was precipitated with cold ether, dissolved in 20% acetonitrile (ACN) containing 2% acetic acid and injected to a Luna 19x250nm/10 μm C8 column (Phenomenex, Torrance, CA) to purify with 0.1%TFA/ACN eluent solvents. Peptide molecular weight characterization was measured by liquid chromatography–mass spectrometry on an Agilent 1260 Infinity/6120 Quadrupole instrument with a Kinetex C8 column with an eluent gradient of 10%–80% 0.05% ACN. The purified peptide (>95% HPLC) measured molecular weight was 2973.0 for the theoretically calculated IUB396 molecular weigh 2973.2.

Vps37a silencing via LNPs

LNPs containing siRNA targeting Vps37a or luciferase as the control were manufactured by Axolabs. Vps37a: sense 5′-cguAcAG AuuAGAauGAcAdTsdT-3' antisense 5′-UGUcAUUCuAAUCUGuACGdTsdT-3'; luciferase: sense 5′-cuuAcGcuGAGuAcuucGAd TsdT-3′, antisense 5′-UCGAAGuACUcAGCGuAAGdTsdT-3′. A, G, U, C are RNA nucleotides; dA, dG, dT, dC are DNA nucleotides; a, g, u, c are 2′-O-methylated nucleotides; s: phosphorothioate. siRNA design, formulation and characterization were performed as described previously (Seitz et al., 2019).

In vivo injections

Eight-week-old male C57BL/6N mice, 12 to 30 weeks old male GCGR knockout mice (C57BL/6 background) and heterozygous control male littermates or male C57BL/6N mice fed a HFD for 13 weeks (starting at the age of 7 weeks) received either PBS or siRNA in LNP formulations (either Vps37a or luciferase control) at 0.5 mg/kg via tail vein injection as described previously (Seitz et al., 2019; Zeigerer et al., 2012, 2015). Pyruvate tolerance tests (PTTs), intraperitoneal glucose tolerance tests (ipGTTs), Glucagon stimulation test (GST) and glycerol stimulation test were performed in C57BL/6N mice 11 d post-injection using 2 g/kg pyruvate, 2 g/kg glucose, 16 μg/kg glucagon or 2g/kg glycerol, respectively, after starvation of 16 h for PTT, glycerol tolerance test and GST or 6 h for GTT. On day 11 post-injection, after 6 h fasting, mice were killed using cervical dislocation and serum and tissue were collected and snap-frozen in liquid nitrogen. For p-Creb, glycogen and cAMP measurements, mice were killed and liver tissue collected by freeze clamping. HFD mice were treated with biweekly injection of LNPs starting at beginning of HFD.

To study insulin sensitivity of the liver, mice starved for 6 h were injected with 0.75 U/kg insulin or PBS and killed after 7 min, freeze clamping Liver, WAT and GC muscle for immunoblot analysis.

Glucagon receptor antagonist, IUB396 (3 nmol/kg) or PBS were injected intra-peritoneal 15 minutes prior to glucagon injections (16 μg/kg) and PTT was performed as previously described. Glucagon (16 μg/kg) or PBS were injected in 16h fasted mice as described above for GST and liver was freeze clamped 20 min after stimulations.

For overexpression experiments, 7 weeks old C57BL/6N mice (WT) fed a regular chow diet were injected with $5x10^{10}$ genome copies (GC) into the tail vein. On week 8 after AAV injection, mice were sacrificed as described above.

Serum parameters

To measure albumin, ALT, Apo A, Apo B, AST, total cholesterol, HDL, LDH, LDL, total protein and triglyceride serum levels, luciferase control and Vps37a knockdown mice were killed 11 d post LNP injection and blood collected from male C57BL/6N mice or mice fed

HFD for 16 weeks. Serum was acquired by centrifugation (10 min, 10,000 *g*). Parameters were measured using the Beckman Coulter AU480 Chemistry Analyzer.

Amino acid measurements by MS/MS

For the measurement of the amino acids and the acylcarnitines a 4.7 mm disk was punched out of a blank filter card (Whatman 903 paper) in a 96-well-filterplate. A total of 5 μL plasma or serum were given onto the disk and dried overnight at room temperature. Sample preparation was performed with the reagents of the MassChrom Kit for analysis of Amino acids and Acylcarnitines from dried blood for Newborn Screening (57000F, non-derivatized, Chromsystems Instrument and Chemicals GmbH, Graefelfing, Germany) with the following steps: 150 μL of a dilution of the Internal Standards (Internal Standard – Succinylacetone:internal Standard, 1:1, v:v) and 75 μL of the Extraction Buffer – Succinylacetone were given onto the disk. The analytes were extracted by 30 min incubation at 45 °C and 600 rpm on a thermoshaker. After centrifuging at 3,200 g for 2min in a 96-wellplate (V-bottom), 10 μL of the supernatant was injected into the MS/MS system via flow-injection (FIA-MS/MS).

Triglyceride and VLDL secretion assay

To measure the amount of triglycerides stored in the liver of luciferase and Vps37a knockdown mice, liver tissue was frozen in liquid nitrogen 11 d after LNP injection and the triglyceride level quantified with the triglyceride assay kit, according to the manufacturer's instructions.

To determine *in vivo* VLDL-TG secretion, Tyloxapol (Triton WR1339) was injected intravenously (500 mg/kg) in 16h fasted mice. Blood samples were collected at 0, 45, 90, 135, 180 and 360 minutes post Tyloxapol injection and plasma TG levels were quantified with the triglyceride assay kit from Abcam, according to the manufacturer's instructions.

Quantitative RT–PCR analysis using SYBR Green

Human or mouse liver tissue or cultured primary hepatocytes were lysed to isolate total RNA using TRIzol. Quantity and integrity of RNA was monitored with a NanoVue Plus Spectrophotometer (GE Healthcare Life Sciences); 1 μg total RNA from liver tissue samples was reverse-transcribed to cDNA using the QuantiTect Reverse Transcription Kit from Qiagen. RT–PCR was conducted in 10 μl of total reaction volume containing SYBR Green, 200 nM of forward and reverse primers (Table S5) and 24 ng of total cDNA. The reaction was performed using the QuantStudio6 system with the following thermal cycling conditions: 50 °C for 2 min; 95 °C for 10 min; 95 °C for 15 s; and 60 °C for 1 min (40 cycles). Relative mRNA levels were quantified by calculating the comparative $2^{-\Delta\Delta Ct}$ method.

Human *VPS37A* mRNA expression studies

Human *VPS37A* mRNA expression was measured by quantitative real-time RT-PCR in a fluorescent temperature cycler using the TaqMan assay, and fluorescence was detected on an ABI PRISM 7000 sequence detector (Applied Biosystems, Darmstadt, Germany). Total RNA was isolated using TRIzol. Quantity and integrity of RNA was monitored with NanoVue plus Spectrophotometer (GE Healthcare, Freiburg, Germany). 1 μg total RNA from liver tissue samples was reverse-transcribed with standard reagents (Life technologies, Darmstadt, Germany). cDNA was then proceeded for TaqMan probe-based quantitative real-time polymerase chain reaction (qPCR) using the QuantStudio 6 Flex Real-Time PCR System (Life Technologies, Darmstadt, Germany). mRNA expression was measured by quantitative real-time RT-PCR using human the following probe for *VPS37A* (Hs01001503_g1). Fluorescence emissions were monitored after each cycle. Human *VPS37A* mRNA expression was calculated relative to the mRNA expression of *18S rRNA* (Hs99999901_s1).

Immunoblot and quantification

Liver tissues or cultured primary hepatocytes were lysed with modified RIPA buffer (20 mM Tris, pH 7.5 (Roth), 150 mM NaCl (Roth), 1 mM EDTA (Roth), 1% SDS, 0.1% Triton-X100 (Sigma-Aldrich), 1% DTT (Sigma-Aldrich) or SDS lysis buffer (20 mM Tris, pH 7.5 (Roth), 150 mM NaCl (Roth), 1 mM EDTA (Roth), 1 mM EGTA (Sigma-Aldrich), 1% SDS, 1% sodium deoxycholate (Sigma-Aldrich)) supplemented with PhosSTOP and EDTA-free protease inhibitor cocktail, respectively. 20-40 μg of cell lysates were subjected to SDS–PAGE gels (Novex WedgeWell 8–16% or 4-20% Tris-Glycine Mini Gels; Thermo Fisher Scientific), transferred to nitrocellulose membranes and incubated with different antibodies (see the antibody and reagents section). Protein bands were detected with Amersham ECL Prime with a ChemiDoc MP Imaging System (Bio-Rad Laboratories) and quantified with Image Lab (Bio-Rad Laboratories) and ImageJ (National Institutes of Health (NIH) using the method outlined at http://lukemiller.org/index.php/2010/11/-analyzing-gels-and-western-blots-with-image-j.

For cytosol and membrane purifications, liver tissues were lysed with homogenization buffer (50 mM Tris-HCl, pH 7.8, 150 mM NaCl, 1 mM MgCl2, 5 mM KCl, 1 mM DTT), supplemented with PhosSTOP and EDTA-free protease inhibitor cocktail using a glass douncer. Liver lysate was centrifuged at 500 g for 20 min at 4 °C to pellet unbroken cells and cellular debris. Supernatant was loaded onto the top of a 30% sucrose and centrifuged at 100,000 g for 1 h at 4 °C. The pellet was resuspended with solubilization buffer (Tris-HCl, pH 8.0, 150 mM NaCl, 1% Triton x-100, 1% SDS and 1 mM DTT) and collected as membrane fraction. The supernatant was collected as cytosolic fraction.

Pulldown assay

Rosetta (DE3) *Escherichia coli* competent cells were transformed with pGEX6P1-DEST (Addgene). A GST-Vps37a expression construct was generated by cloning mVps37a from pdsAAV2-LP1-mVps37a, described above, using KnpI and NotI. Expression of GST-Vps37a was induced by 1 mM IPTG at an optical density (600 nm) of 0.5 and bacteria were incubated for 4 h at 37°C. Bacteria pellet was resuspended in phosphate-buffered saline (PBS, Merck Millipore) and supplemented with 100 μg/mL lysozyme for 30 min on ice. After adding 0.1 mM PMSF and 1 mM DTT, bacteria lysate was sonicated at an amplitude of 50 % for 5 min (30 sec sonication and 30 sec break). GST-Vps37a was purified on a GSTrap HP 5 mL column (Cytiva) using the ÄKTA pure 25 system (Cytiva) according to manufacturer's instructions. In short, prepared bacteria lysate was filtered through a 0.45 μm polyvinylidene difluoride (PVDF) Whatman GD/X filter (Cytiva) and loaded on the pre-equilibrated column at a flow rate of 5 mL/min. Recombinant GST-Vps7a was eluted using a linear gradient of 0-100% elution buffer (50 mM Tris/HCl pH 8.0, 10 mM reduced glutathione) in 5 column volumes.

For GST-pulldown experiments, purified GST-Vps37a and GST only were coupled to Glutathione Sepharose 4B (GE Healthcare Life Science). Liver tissue from mice was prepared in CHAPS buffer (20 mM HEPES pH 8.0, 150 mM NaCl, 0.3% CHAPS) supplemented with protease and phosphatase inhibitors (Roche cOmplete). Tissue was homogenized at 4 ms speed for 20 sec (Omni Bead Ruptor 24), filtered through a 0.45 μm PVDF membrane (Ultrafree-CL, Merck Millipore) and protein concentration was adjusted by BCA assay. For protein binding, mouse liver lysates were incubated on GST-Vps37a and GST only beads overnight at 4°C while rotating. Beads were washed 5 x in CHAPS buffer and proteins were eluted in sample buffer (200 mM Tris/HCl pH 6.8, 6% SDS, 20% glycerol, 0.1 g/mL DTT, 0.01 mg bromophenol blue) for 5 min at 95°C followed by detection in immunoblotting.

Histology

Liver samples of luciferase control and Vps37a knockdown mice were collected 11 d after LNP administration at 16 weeks of HFD or chow diet and snap-frozen in liquid nitrogen. Excised specimens were fixed in 4% (w/v) neutrally buffered formalin (Sigma-Aldrich), embedded in paraffin (SAV LP) and cut into 3-μm slices for hematoxylin and eosin (H&E) staining or for immunohistochemistry. Immunohistochemical staining was performed under standardized conditions on a Discovery XT automated stainer (Ventana Medical Systems). The stained tissue sections were scanned with an Axio Scan.Z1 digital slide scanner (ZEISS) equipped with a 20× magnification objective. Images were evaluated with the commercially available image analysis software Definiens Developer XD2 (Definiens) following a previously published procedure (Feuchtinger et al., 2015). The calculated parameter was the mean area occupancy of the lipid droplet describes as % lipid content the stained tissue.

For cryostat sections, control and Vps37a knockdown mice were perfused with PBS to clear the veins off blood and perfused with 4% paraformaldehyde (PFA) for at least 15 minutes. Liver was then excised, rotated in 4% PFA at 4 °C overnight and placed in PBS until further use. Before embedding them in optimal cutting temperature compound, liver specimens were transferred to 30% sucrose for 3 d. Then, 5–7 μm cryostat sections were cut and collected on Superfrost Plus-treated slides. Cryosections were immunolabelled with first antibodies incubated in PBS BSA (3%) for 2 h and secondary antibodies (1:1000), Bodipy (1:1000) and phalloidin (1:400) for 1 h at room temperature. Then, sections were washed with PBS, incubated with 4,6-diamidino-2-phenylindole (DAPI, 1:10000) for 5 min and mounted with 0.1 g ml^{-1} MOWIOL 4-88 reagent onto coverslips.

Hepatocyte isolation and transfection

Primary hepatocytes were isolated via collagenase perfusion from 8–12-week-old male C57BL/6N mice (Zellmer et al., 2010). Briefly, mice were anaesthetized, both abdominal walls were opened and the liver was perfused through the *venae cavae* with EGTA-containing HEPES/KH buffer for 10 min, followed by a collagenase-containing HEPES/KH buffer for 10–12 min until liver digestion was visible. The perfused liver was cut out and placed into a suspension buffer-containing dish and hepatocytes were gently washed out. After filtering the cells through a 100-nm pore mesh, cells were centrifuged and washed twice and resuspended in suspension buffer. For a detailed isolation protocol including pictures, please see Godoy et al. (2013).

200,000 cells per well were plated in collagen-coated 24-well plates in William's Medium E containing 10% FCS (PAN-Biotech), 5% penicillin-streptomycin and 100 nM dexamethasone and maintained at 37 °C and 5% CO_2. After 1 h, cells were washed with PBS and incubated with 30 nM siRNA (Vps37a/β-arrestin-2) and interferin (1.2 μl $well^{-1}$) in William's Medium E. For the double knockdown of Vps37a and β-arrestin-2, cells were incubated with 60nM of siRNA (30nM Vps37a plus 30nM β-arrestin-2 siRNA and 60 nM control). After 6 h of incubation, cells were washed with PBS and a second layer of collagen was added to maintain cells in a sandwich culture. William's Medium E was changed every other day (Zeigerer et al., 2015, 2017).

Cryopreserved primary human hepatocytes were purchased from Lonza Group Ltd and cultured on collagen-coated 24-well plates in Williams Medium E as described for the mouse primary hepatocytes above.

Stimulation experiments in primary mouse hepatocytes

Glucagon stimulations were performed by treating the cells, 4 days after RNAi, with 100 nM glucagon or vehicle for 5 min (PKA) and 15 min (p-Creb) after 2 h starvation with FBS- and DEX-free William's Medium E. For the *in vitro* experiments with glucagon receptor antagonist IUB396, cells were pretreated with IUB396 (10 μM) for 15 min followed by treatment with 100nM of glucagon. For transcript level changes after glucagon stimulations, cells were treated after 4 days of RNAi with 100nM glucagon for 5 h in FBS- and DEX-free William's Medium.

The time course of p-Creb degradation was performed by treating the cells after 4 days of RNAi and 2 h starvation in FBS- and DEX-free William's Medium E, with 100 nM of glucagon for 10 min followed by PBS-wash and collecting cell lysates at 5, 15, 30, 60, 90 and 120 min.

Isoproterenol and forskolin treatments were performed by treating the cells with 10 μM of forskolin or Isoproterenol for 5 min after 2 h starvation with FBS- and DEX-free William's Medium E.

HFD *in vitro* conditions were obtained by supplementing William's Medium E with 100 μM palmitate and 500 μM oleate (both conjugated with BSA 1:6) (Sigma-Aldrich) or the respective amount of BSA and cells were stained with Bodipy (3.8 μM, 1:1000).

Ligand-Induced BRET Assays

HEK293T cells (700,000/well) were seeded in 6-well plates and incubated to 70% confluency in DMEM (10% FBS, 1% Pen/Strep). Twenty-four hours following seeding, transient transfections were performed using Lipofectamine 2000 according to the manufacturer's protocol, and were then incubated for twenty-four hours. Transfections consisted of 1.5 μM of control or Vps37a siRNA, including co-transfection with: 500ng/well GcgR-GFP and 50ng/well mini Nluc-Mini$G_{\alpha s}$ (G-protein recruitment to the receptor), 300ng/well GcgR-untagged and 500ng/well Gβγ-BERKY3 (indirect quantification of GTP-Gα formation), and 300ng/well GcgR-untagged, 50ng/well min Nluc-Mini$G_{\alpha s}$, and 500ng/well Venus-Rab5a (early endosomes Gα co-localization). Following transfection, HEK293T cells were washed with PBS and resuspended in FluoroBrite phenol red-free complete media, and plated into poly-D-Lysine-coated 96-well white polystyrene LumiNunc plates. BRET assay were performed using NanoLuciferase substrate NanoGlo. BRET measurements were taken every 30 seconds using a PHERAstar FS multi-mode microplate reader. Ligand-induced (1 μM glucagon) measurements on the temporal scale are represented as the subsequent measurement after time point zero. Each experiment was independently performed at least three times, with at least three technical replicates for each group. Untagged GcgR and GcgR-eGFP were purchased from BioCat GmbH (Heidelberg, Germany). Venus-Rab5a (early endosomes) and NES-Nluc-Mini-$G_{\alpha s}$ were kind gifts from Professor Kevin Pfleger (Harry Perkins Institute of Medical Research, Nedlands, WA, Australia) as originally published by Professor Nevin Lambert (Augusta University, Augusta, GA, USA) (Lan et al., 2011; Wan et al., 2018). Gβγ-BERKY3 was a gift from Mikel Garcia-Marcos (Maziarz et al., 2020).

Immunofluorescence, EGF uptake assay and Cy5-glucagon incubations

For IF, cells in sandwich cultures were fixed 4 d post-plating in 4% PFA at room temperature for 30 min, subsequently washed twice with PBS, permeabilized for 1 h with 0.1% Triton X-100 (AppliChem, Darmstadt, Germany), and washed and blocked for 2 h in 10% horse serum (Thermo Fisher Scientific, Waltham, MA) (Zeigerer et al., 2017). Overnight, cells were incubated with primary antibodies at room temperature, washed for 2-4 h with Tris HCl (pH 8.0, 10 mM; Roth, Karlsruhe, Germany) and NaCl (300 mM; Roth, Karlsruhe, Germany) Tween solution (0.1%) (Sigma-Aldrich Chemie Munich, Germany) and incubated with secondary antibodies (1:1000) and phalloidin (1:400) for 5 h at 37 °C. Cells were washed twice with PBS, incubated with DAPI (1:10,000) for 5 min then mounted onto glass slides with 0.1 g/ml MOWIOL 4-88 reagent.

Cells in monolayer culture were fixed for 15 min in PFA, washed twice for 5 min in PBS and permeabilized in 0.1% Triton X-100 in PBS for 10 min at room temperature. After two more washes for 5 min in PBS, cells were blocked in 10% horse serum for 10 min at room temperature and subsequently treated with primary antibodies in 5% horse serum for 1 h. Cells were washed 3 times for 5 min in PBS and incubated for 1 h with secondary antibodies (1:1000) at room temperature. Subsequently, cells were washed twice with PBS and stained with DAPI, then mounted onto glass slides with 0.1 g/ml MOWIOL 4-88 reagent.

For the EGF uptake assay, cells were starved for 2 h in William's Medium E without serum or dexamethasone. Continuous uptake of alexa555-EGF (200 ng/ml; continuous uptake) for several time points was performed, cells were washed with cold PBS and fixed in 4% PFA (Zeigerer et al., 2012). Cells were stained with DAPI and mounted with MOWIOL 4-88 reagent.

For surface detection of glucagon receptor, cells were placed on ice, washed with ice cold PBS and incubated with Cy5-glucagon (200 nM) for 2 h in William's Medium E without serum or dexamethasone. After, cells were washed again in ice cold PBS and fixed in 4% PFA for 30 min. For intracellular localization of glucagon receptor, cells were simultaneously incubated with alexa555-EGF (200 ng/ml) and Cy5-glucagon (1000 nM) for 6 h followed by PBS and fixation in 4% PFA for 30 min. For the glucagon receptor trafficking studies in mouse and human primary hepatocytes, cells were incubated with Cy5-glucagon (1000 nM, 0.2μM filtered) for 2h, washed with PBS and fixed with 4% PFA for 30 minutes, followed by immunofluorescent staining with either EEA1, Lamp1, Rab11 or Vps37a as described above. Cells were stained with DAPI and mounted with MOWIOL 4-88 reagent.

Confocal microscopy and analysis

Immunofluorescent samples were analyzed using a laser scanning confocal microscope (Olympus FluoView 1200; Olympus Corporation) equipped with an Olympus UPlanSAPO ×60 1.35 and an UPlanSAPO ×40 1.25 solid immersion lens oil immersion objective (Olympus) at a resolution of approximately 100 $\mu m\ pixel^{-1}$ (×60) and 600 nm step size. Quantifications were performed for individual images after background subtraction with a minimum of 30 cells using Fiji software (ImageJ, v.2.0.0-rc-69/1.52p). For background subtraction, the ImageJ rolling ball function was run on the images with a radius of 50 without any options. Nuclear and total intensity were measured per cell by using the ImageJ freehand selection and a Region of interest (ROI) tools. For calculation of nuclear to total ratio, the mean nuclear intensity was divided by the mean total intensity.

Vesicle 3D Reconstruction, PSC coefficients and Co-localization threshold analysis and statistics

For quantification of the co-localization between signals from Cy5-glucagon/EGF Pearson and Spearman Correlation coefficients (PSC) were calculated by using the PSC co-localization plug-in of ImageJ 1.52e (National Institutes of Health) according to French et al. (2008). At least 10 individual cells in three independent images and a minimum of 500 signals were considered for every analysis. Calculated PSC values were between −1 (negative correlation) and +1 (positive correlation) and the threshold level, under which pixels were treated as background noise, was set at 10. The results were presented as scatter plots with Pearson's and Spearmann's coefficients (r_p and r_s).

For quantification of the level of colocalization between signals from Cy5-glucagon with Vps37a, EEA1, Lamp1 or Rab11, images were deconvolved using the FIJI plugins point spread function (PSF) generator (Kirshner et al., 2013) and DeconvolutionLab (Sage et al., 2017) (EPFL; http://bigwww.epfl.ch/). Z-step was set to 0.6 μm and a PSF algorithm (Born & Wolf 3D Optical model) was used for PSF generation. The generated PSF and a 3D deconvolution algorithm (Richardson-Lucy with TV regularization) were applied to images using DeconvolutionLab. The co-localized pixel map was then generated by using the colocalization threshold of ImageJ. The generated map was split into three channels, two original and the colocalization images. Then fluorescent dots in each image were counted by using particle analysis plug-in of ImageJ. The fluorescent dots with a pixel from 0.1 to 10 and circularity from 0.0 to 1.0 were included in the analysis. The colocalization rate was calculated by dividing the number of fluorescent dots in the colocalization image by the number of entire fluorescent dots from Cy5-glucagon, Vps37a, EEA1, Lamp1 or Rab11.

β-oxidation assay with Seahorse

Fatty acid β-oxidation was measured using the Seahorse XFe 24 Analyzer (Agilent Technologies). Therefore, 30,000 cells per well were plated as a monolayer culture in Seahorse cell plates precoated with collagen. Oxidative phosphorylation was conducted 2 d after siRNA knockdown of luciferase control or Vps37a after 24 hours of substrate starvation. Cells were treated just prior to the assay with either BSA or Palmitate Substrate (Agilent Technologies) as suggested by the manufacturer and oxidative phosphorylation measured after injection of 2 μM oligomycin (Sigma-Aldrich), 1 μM FCCP (Sigma-Aldrich) and 1 μM antimycin A (Sigma-Aldrich) + 1 μM rotenone (Sigma-Aldrich). Glucagon stimulations were performed by treating the cells with 100 nM glucagon (Millipore) for 24 hours prior to the assay.

Glucose secretion assay

The glucose secretion assay from primary hepatocytes was adapted from Sakai et al. (2012). Primary hepatocytes three days after RNAi were starved in phenol-free DMEM for eight hours containing 0.5% FBS, 5 mM glucose, 4 mM glutamine. Afterwards, the cells were washed twice with PBS at room temperature and stimulated with DMEM containing 4 mM glutamine, 2 mM pyruvate, 20 mM lactate +/- 10 nM glucagon, 100 nM Dexamethasone and 1 μM forskolin for 12 hours. Medium was collected and glucose content measured using an Amplex Red glucose assay kit. The remaining cells were lysed to measure protein content for well-based normalization.

Cholesterol secretion assay

Primary murine hepatocytes in collagen sandwich cultured in Williams Medium E without dexamethasone were washed and serum-starved for 5 h on d4 after RNAi. Medium was collected and amounts of cholesterol in the supernatant were measured according to the manufacturer's instructions using the Amplex Red Cholesterol Assay Kit. Secreted amounts of cholesterol were normalized to total protein levels, determined using the DC Protein Assay kit (Bio-Rad Laboratories), as described previously (Seitz et al., 2019).

cAMP, glycogen and insulin measurements

Freeze clamped liver tissues from control and Vps37aKD mice, after 11 days LNP treatment and 6h starvation, were utilized to measure cAMP (cAMP direct immunoassay kit (abcam)) and glycogen (glycogen assay kit (Sigma)) according to manufacturer's protocol. Plasma glucagon concentrations were measured by mouse glucagon ELISA (Mercodia) according to manufacturer's protocol. Serum insulin content from chow- or HFD-fed animals was assessed by a mouse insulin ELISA (Alpco) according to the manufactures protocol.

QUANTIFICATION AND STATISTICAL ANALYSIS

Statistical analyses were performed in GraphPad Prism v8 and data was plotted using KaleidaGraph v5. Standard deviation was assumed equal between experimental groups. Two-tailed, unpaired Student's t tests were performed to calculate statistical significance. $p < 0.05$ was considered statistically significant. The mean ± SEM are shown in the figure legends. *$p < 0.05$, **$p < 0.01$, ***$p < 0.001$, ****$p < 0.0001$, *****$p < 0.00001$. Only data that reached statistical significance are indicated.